Alma Mater Studiorum
Università di Bologna

Master Advanced Spectroscopy in Chemistry
Master's Thesis

Synthesis and Characterization of Hydroxyapatite Modified with (9*R*)-9-Hydroxystearic Acid

Author:
Luíza Mamigonian Bessa

Supervisor:
Dr. Maria Cristina Cassani
Co-supervisors:
Dr. Carla Boga
Dr. Elisa Boanini

June 25, 2014

Abstract

(9*R*)-9-hydroxystearic acid (9R-HSA) has been proven to have antitumoral activity because it is shown to inhibit histone deacetylase 1, an enzyme which activates DNA replication, and the (*R*)-enantiomer has been shown to be more active than the (*S*)-enantiomer both *in vitro* and by molecular docking. Hydroxyapatite is the main mineral component of bone and teeth and has been used for over 20 years in prostheses and their coating because it is biocompatible and bioactive. The goal of incorporating 9R-HSA into hydroxyapatite is to have a material that combines the bioactivity of HA with the antitumoral properties of 9R-HSA.

In this work, 9R-HSA and its potassium salt were synthesized and the latter was also incorporated into hydroxyapatite. The content of (9*R*)-9-hydroxystearate ion incorporated into the apatitic structure was shown to be a function of its concentration in solution and can reach values higher than 8.5%. (9*R*)-9-hydroxystearic acid modified hydroxyapatite was extensively characterized to determine the effect of the incorporation of the organic molecule. This incorporation does not significantly alter the unit cell but reduces the size of both the crystals as well as the coherent domains, mainly along the *a*-axis of hydroxyapatite. This is believed to be due to the coordination of the negatively charged carboxylate group to the calcium ions which are more exposed on the (100) face of the crystal, therefore limiting the growth mainly in this direction. Further analyses showed that the material becomes hydrophobic and more negatively charged with the addition of 9R-HSA but both of these properties reach a plateau at less than 5% wt of 9R-HSA.

Contents

List of Figures

List of Tables

1 Introduction

1.1 Cell Cycle and Tumors

The cell cycle (Figure 1) is the series of events that lead up to cell division. Generally it is split into two main phases: mitotic (M) phase, where the actual splitting of the cells occur, and the interphase, where the cell grows and the DNA is replicated. The interphase is considered to be split into 3 phases, two gap phases called G_1 and G_2, where cell growth occurs and many proteins are synthesized, separated by a phase called S (Synthesis) phase where the DNA replication occurs. There is also another gap phase called G_0 where the cell leaves the cycle and arrests its division permanently or temporarily. Between these phases there are checkpoints that control the passing of the cell between one phase and the other. The most important ones for cell division are the G_1/S and G_2/M between those respective phases.[1]

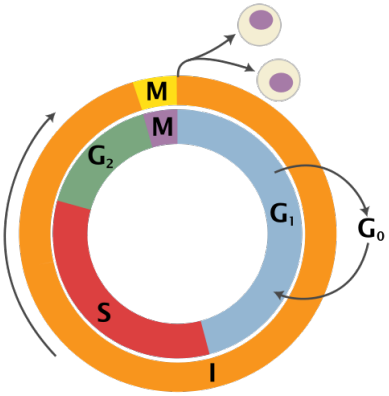

Figure 1: General scheme of the cell cycle. It is split into interphase (I) and mitotic (M) phase, the interphase is further split into gap phases (G_1 and G_2) and synthesis (S) phase.

A tumor or neoplasm is tissue resulting from an abnormal growth of the cells. This growth is greater and not coordinated to that of the surrounding normal tissue. Neoplasms can be benign or malignant and in this last case are called cancer or tumors.
Tumor cells have uncontrolled growth because the control mechanisms that avoid replication of damaged cells stop working. This is almost always due to a change in one or more genes, changing the function of the proteins they produce, resulting in faulty cell cycle control. This usually can be seen as a problem with the genes relative to the two checkpoints.[1]

p53 is a protein that is shown to be mutated or inactive in many tumor cells. It is activated when the cell recognizes stressors like DNA damage, oxidative stress and oncogene expression. It is related to many pathways with anti-cancer functions: activate DNA repair, arrest the cell cycle at the G_1/S checkpoint and initiate apoptosis. One of these pathways is by activating the expression of the $p21^{WAF1}$ protein. This protein binds to cyclin dependent kinases (CDK) necessary for the G_1/S transition. The effect of 9-hydroxystearic acid on these pathways has been a subject of recent research.[2–4]

1.2 9-Hydroxystearic Acid

9-Hydroxystearic acid (9-HSA, Figure 2) is an organic fatty acid. In this work it is synthesized from the unsaturated dimorphecolic acid, also known as, (9*S*,10*E*,12*E*)-9-hydroxyoctadeca-10,12-dienoic acid. Dimorphecolic acid (Figure 3) is the main fatty acid found in *Dimorphotheca sinuata* L. seeds (Figure 4) amounting to about 65% of the total fatty acids found in the seeds of this genus.[5]

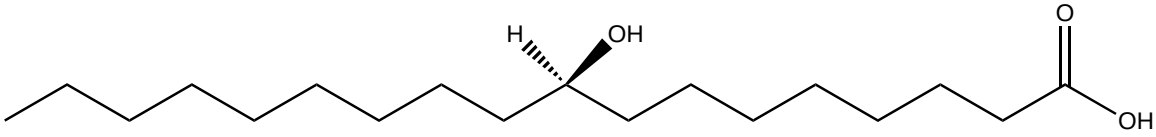

Figure 2: 9*R*-Hydroxystearic Acid or (9*R*)-*R*-hydroxyoctadecanoic acid.

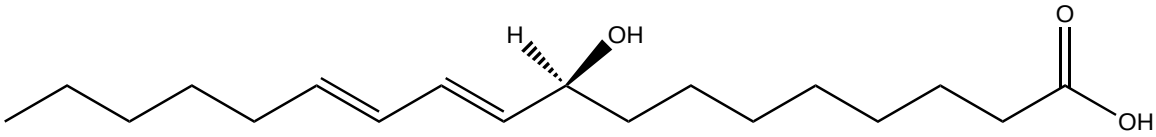

Figure 3: Dimorphecolic acid or (9*S*,10*E*,12*E*)-9-hydroxyoctadeca-10,12-dienoic acid.

Figure 4: *Dimorphotheca sinuata* L. flowers (left) and seeds(right). The seeds have a high dimorphecolic acid content.

9-HSA is known to derive from lipid peroxidation and believed to be recognized by the cell as a sign of external stress. The synthesis is done by extraction of the oil from the seeds because this is the only source of enantiomerically pure 9R-HSA. Attempts have been made to find a different enantioselective synthesis pathway, chiefly through enzymatic kinetic resolution but these have been proven difficult due to the high symmetry of the molecule.[6] A racemic mixture of 9-HSA can be produced after hydrolysis of the methylester, starting from commercially available mono-methylazelate, by the pathway shown in Figure 5.[7]

9-HSA is a byproduct of lipid peroxidation. Lipid peroxidation is caused by radical reactions like those triggered by reactive oxygen species that are formed during cellular respiration. It is a mechanism for the deterioration of fats and oils within cells and generally is seen in cellular

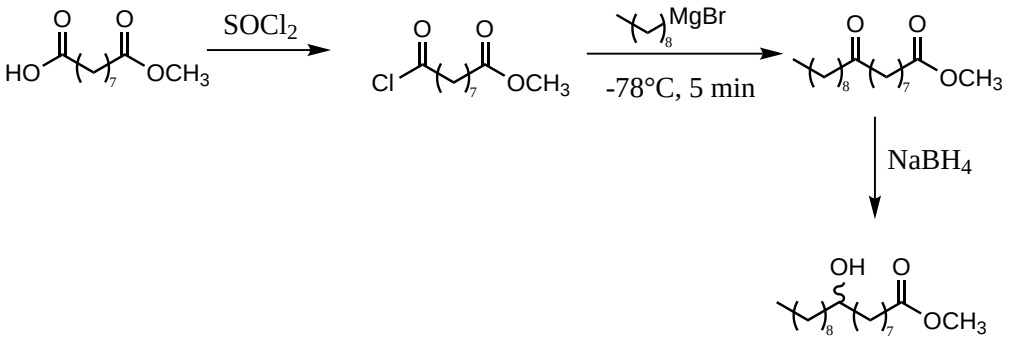

Figure 5: Reaction scheme for the synthesis of methyl (*R*,*S*)-9-hydroxystearate.

membranes. Peroxidized lipids can become more hydrophilic, diffuse to other parts of the cell and cause damage farther from the source. In tumor cells the intermediates of lipid peroxidation, as well as the polyunsaturated fatty acid content in membrane lipids, are reduced. It has been shown that lipid peroxidation products stall cell proliferation and can induce cell death.[8] Since 9-HSA is a lipid byproduct that is seen in lower quantities in tumor cells, it was an interesting molecule to test for its anti-tumor activities.

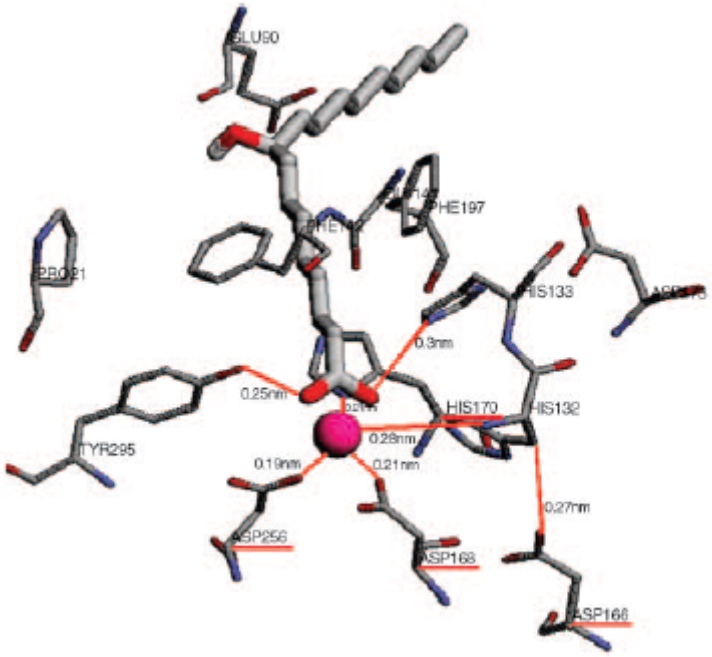

Figure 6: Binding of 9R-HSA to zinc-dependent human HDAC1 protein.[9]

A few studies of 9-HSA on different cell lines have been carried out. Firstly, in C108, a murine Lewis lung carcinoma cell line, 9-HSA and 10-HSA were isolated and proven to exist in mammalian cells.[10] In the T leukemia cell line Jurkat J6 (J6)9-HSA was able to elicit Activation Induced Cell Death (AICD) in concentrations above 10 μM by activation of caspase 3. At 5 μM no significant apoptosis was detected but significant inhibition of proliferation due to an increase in the percentage of cells in G_0/G_1 and a decrease in S phase. This was said to be due

to changes in the expression of cyclin D3 and hypophosphorilated pRB.[2]

Most studies were done with HT29, a human colon adenocarcinoma cell line. One of the particularities of this cell line is that it has a mutated inactive p53 gene so experiments with this cell line indicate a p53-independent pathway. 9-HSA is shown to be cytostatic in HT29 in a pathway that depends on $p21^{WAF1}$ because this result is not observed in the $p21^{WAF1}$-deleted HCT116 human colon carcinoma cells.[11] It causes the arrest of the cell cycle in G_1 phase. In another study[4] it was shown to act as a HDAC1, HDAC2, HDAC3 inhibitor. Histone deacetylase 1 (HDAC1) deacetylates lysine groups on chromatin, allowing it to bind more strongly to DNA and stimulate DNA synthesis, therefore histone deacetylase inhibitors are interesting as prospective anti-tumor drugs. 9-HSA induces in this cell line an increase of p21 transcription and lower expression of cyclin D1,[4] which is known to regulate the G_1/S transition. A docking experiment (Figure 6) showed that 9-HSA binds to HDAC1 and that the *R*-enantiomer is more active than the *S*-enantiomer.[9] This was also confirmed in cells.[4]

It has been shown in U2OS, a human osteosarcoma line with an active p53 gene, that 9-HSA also affects p53 by inducing hyperacetylation due to its HDAC1 inhibitory activity. This induces apoptosis by a mitochondrial pathway.[3]

1.3 Hydroxyapatite

Hydroxyapatite or hydroxylapatite (HA, Figure 7) is a mineral from the apatite group of phosphates presenting the formula $Ca_{10}(PO_4)_6(OH)_2$. The other common members of this group include chlorapatite ($Ca_{10}(PO_4)_6Cl_2$) and fluorapatite ($Ca_{10}(PO_4)_6F_2$).

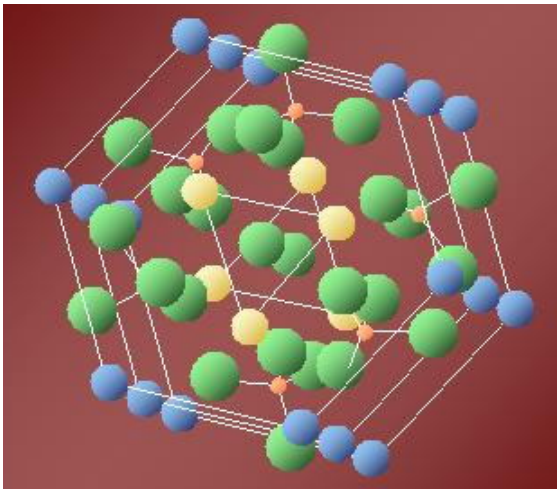

Figure 7: Simplified structure of hydroxyapatite. Ca(I) (in blue) form columns parallel to the *c*-axis and Ca(II) (in yellow) are the vertices of staggered equilateral triangles around the screw axis. Oxygens are shown in green and phosphorus in orange. Hydrogens are omitted for simplicity but are found along the screw axis.[12]

When compared to other calcium phosphates, HA is the most stable[13] and with one of the the highest Ca/P ratio. Stoichiometric HA has a Ca/P ratio of 1.67. Decreasing the Ca/P ratio,

even in mixed materials, results in higher solubility of the calcium phosphate in a physiological environment.[14]

HA has two known crystalline forms. The first one is monoclinic and crystallizes in the $P2_1/b$ space group.[15] The most important form is the hexagonal form which the crystal structure was published by Kay in 1964.[16] It belongs to the $P6_3/m$ space group with unit cell parameters $a = b = 9.432$Å, $c = 6.881$Å, $\alpha = \beta = 90°$ and $\gamma = 120°$.[17] This space group is characterized by its symmetry elements: a sixfold screw axis parallel to the c-axis with a period of $\frac{1}{2}$ and two mirror planes parallel to the ab plane that intersect the c-axis at the $\frac{1}{4}$ and $\frac{3}{4}$ positions. The calcium ions occupy two different independent cation sites, usually named Ca(I) and Ca(II). Ca(I) atoms form a column parallel to the c-axis. Ca(II) form the walls of "channels" along the screw axis, at the vertices of staggered equilateral triangles (Figure 7). The hydroxide ions are aligned within the screw axis, with random directions with respect to the c-axis.

There are several synthetic methods to produce HA in the literature, these differ in the reaction conditions and are usually classified as two main methods. The first one consists of a titration of a calcium hydroxide suspension with phosphoric acid until neutrality.[18] In the second, the precipitation method, a monobasic sodium or ammonium phosphate is added dropwise to a calcium containing solution (usually calcium acetate or nitrate).[19] Both methods produce products with high crystallinity when carried out at 100°. The lowering of the temperature produces an increase of the amount of amorphous material present, therefore, reducing the crystallinity. The precipitation method must be kept basic ($pH > 9$) during the synthesis, usually by the addition of sodium hydroxide or ammonia, favoring the precipitation of HA instead of other calcium phosphates. Reaction time also affects the crystallinity and average crystallite size. If the reaction time is too short the product tends to be nanocrystalline with a large amorphous portion and as it increases, the crystallinity improves.[13] The synthesis is usually carried out under nitrogen, because in air the incorporation of carbonates is significant (and further reduces crystallinity). Finally, apatites, like other calcium phosphates, can be obtained from metastable phosphates in aqueous solution.[20]

The incorporation of divalent cations, anions like F^-, Cl^-, CO_3^{2-} or other molecules can alter several of hydroxyapatite's physicochemical properties, including the cell parameters, morphology and size of the crystals, amount of amorphous material, thermal stability and solubility.[21]

However, the main interest in HA is due to its role in the structure of bone and teeth. HA is the main mineral constituent of bone (70% wt) and teeth (96% wt) usually with a small amount (4–6%) of carbonate being exchanged with the phosphate groups in the structure.[22] HA has been used for over 20 years as dense bioceramics, porous bioceramics, coating for implants or as a powder for gap fillings.[23] HA promotes osteointegration, particularly in its use as a coating for metallic implants.[24,25] The degree of integration depends on the ability of the material to imitate the characteristics of natural bone, including composition, surface and mechanical properties. Its use in prosthetics is particularly interesting within the scope of this work because in many cases the treatment of osteosarcoma includes bone resection and cancer

recurrence is a possible complication.[26] Another possible complication is bacterial infection on the prosthesis and composite materials that include antibiotics[27,28] or silver nanoparticles,[29–31] for their broad antibiotic properties, have been prepared.

1.4 Spectroscopic and Spectrometric Methods

1.4.1 Nuclear Magnetic Resonance

Nuclear Magnetic Resonance (NMR) spectrometry is an absorption spectrometry, much like Infrared and Ultraviolet spectrometries. The wavelength used is in the microwave region. Spin and orbital angular momenta give rise to magnetic moments. Classically the energy of a magnetic moment μ in a magnetic field B^0 is given by Equation 1 and the quantum mechanical equivalent Hamiltonian is equation 2. The magnetic moment operator can be further decomposed and in the case of the nuclear spin to give equation 3 where γ_N is called the gyromagnetic ratio and $\hat{l}$ is the angular momentum operator.[32]

$$E = -\mu B^0 \tag{1}$$

$$\hat{H} = -\hat{\mu} B^0 \tag{2}$$

$$\hat{\mu} = \gamma_N \hat{l} \tag{3}$$

Because the eigenvalues for $\hat{l}$ are $\hbar m_I$ the Hamiltonian can be solved to give rise to Equation 4 where m_I is the value spin magnetic moment. In the absence of an external magnetic field states with different values of m_I are degenerate.

$$E(m_I) = -\gamma_N \hbar m_I B^0 \tag{4}$$

Under a magnetic field, different values of nuclear spin lose their degeneracy. The splitting is called the nuclear Zeeman Effect (Figure 8). This energy difference is usually in the microwave region of the electromagnetic spectrum and this transition is what is observed in an NMR spectrum. The magnitude of the splitting of a certain nucleus is not only dependent on the external magnetic field but actually on the local effective magnetic field. The difference between the external field and the effective field is termed chemical shift and is of major importance when using NMR for organic synthesis. Chemical shift arises from the movement of electrons within the sample, induced by the external magnetic field. Since this movement is an electrical current, it creates a smaller local magnetic field which in turn changes the value of the magnetic field effectively "seen" by a particular nucleus. Chemical shift contains information on the chemical environment and can be associated with chemical functions in proximity of the nucleus, for example.

Another important phenomenon present on a NMR spectrum is the splitting. One particular type of splitting, J-splitting, is commonly used for attributions in organic spectra. This splitting is caused by a slight difference in energy depending on whether the nucleus is aligned or opposed

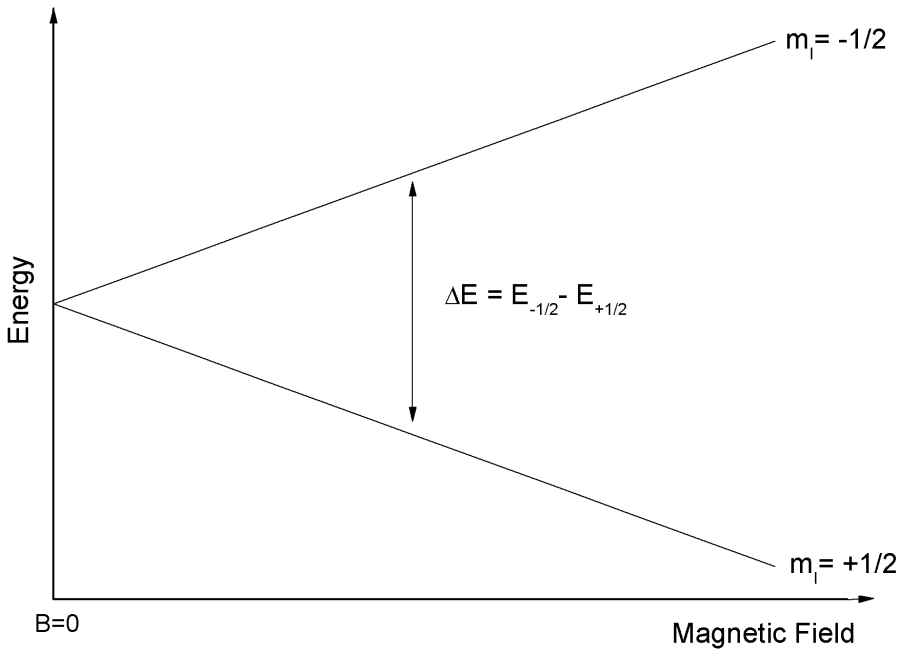

Figure 8: Zeeman Effect: Splitting of the energy levels for a I=1/2 system like ^{1}H or ^{13}C.

to the electrons around it. Since it is due to the local fields created by neighboring magnetic moments it is independent of the external magnetic field, therefore is usually expressed as a frequency (in Hz).

Current routine NMR is done with a setup as shown in Figure 9.

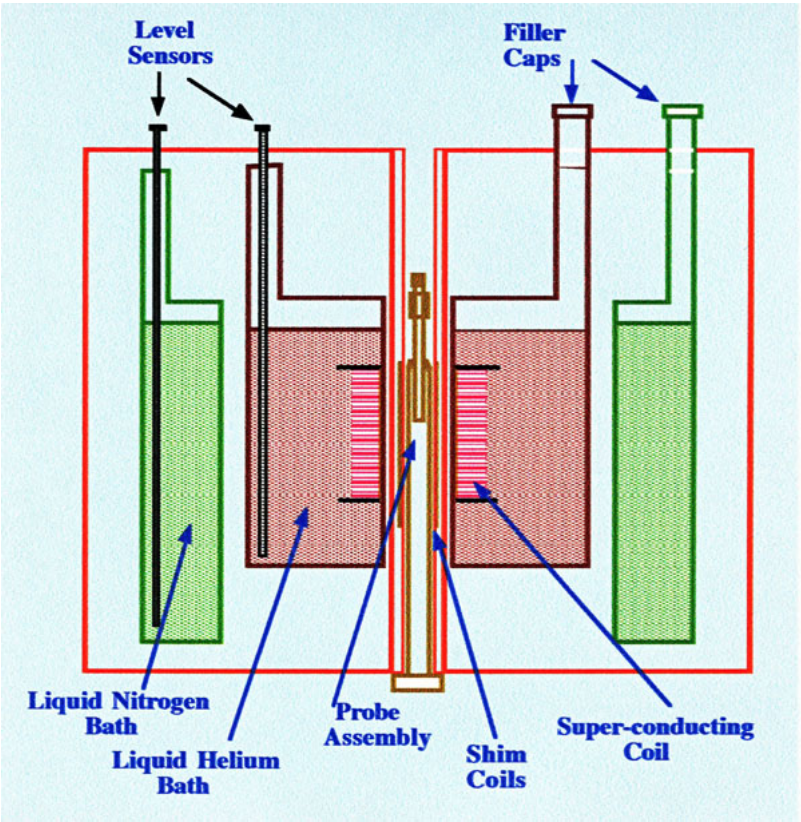

Figure 9: Scheme of a NMR machine using a superconductive magnet.[33]

The main parts are the superconductive electromagnet, the probe and the console. The electromagnet is made up of metal wires wrapped around the probe in a solenoid coil and this produces a homogeneous magnetic field in the sample. The metal wires are cooled down to 4 K to achieve super conductivity using liquid helium. The liquid helium bath is surrounded by vacuum and liquid nitrogen, to avoid evaporation and heat transfer. The probe is the part that produces the radiofrequency pulse that will excite the spins and that detects the precession of the spins. It contains a solenoid of wires, called shim coil, perpendicular to the main magnetic field that is necessary for the pulse and that receives the induced current from the precession motion. The console includes parts of the machine necessary for signal processing. The signal produced by the equipment is called a Free Induction Decay (FID) and must be decomposed into its constituent frequencies by Fourier Transform (FT) to obtain the typical NMR spectrum.

1.4.2 X-Ray Diffraction

Peter Paul Ewald and Max Laue realized in 1912 that crystals could be used as diffraction grating as long as the wavelengths used were shorter than visible light, in the X-Ray portion of the electromagnetic spectrum to be exact. This is because for diffraction to occur, the electromagnetic radiation should be of the same order of magnitude as the spacing in the grating and typical spacing between atoms in a crystal is about 2-3Å. Photons hitting atoms in a crystal will scatter as a wave around the atom and by interacting with the photons scattered by other atoms interference occurs. Most interference is destructive but in few directions the interference is constructive. These directions are given by Bragg's Law (equation 5), where λ is the wavelength of the X-rays being scattered, d is the distance between atomic planes, θ the incident angle and n a positive integer. The reason for this can be seen in Figure 10.[32]

$$n\lambda = 2dsin\theta \tag{5}$$

In the case of a monocrystal, an intense beam of X-rays is directed onto the crystal and causes

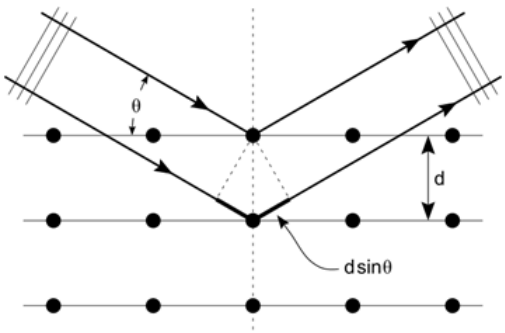

Figure 10: Schematic proof of the Bragg's Law. At a given angle θ, the difference in path length of the X-ray to reach the next plane of atoms is given by 2d sinθ.

a diffraction pattern made up of discrete points which can be recorded using photographic film, a point detector or an area detector like a charge-coupled device (CCD). The intensity of these

points contains information on the motif (nature and position of the atoms) while the position of these points contain information on the unit cell or the matrix of the crystal.[34]
In this work, crystalline powder X-ray diffraction will be used. The powder is made up of many very small crystals with random orientation As a consequence, the position of the diffraction spots changes for each crystallite and the resulting diffraction is composed of circles instead of points. This is usually represented as a diffractogram taken radially (Figure 11). Each peak contains all the families of planes with the same interplanar distance d, this is called the multiplicity of the peak. For example, cubic unit cells have the same interplanar distances in several directions (d_{100}, d_{010} and d_{001}) and will show all of these planes as a single peak.

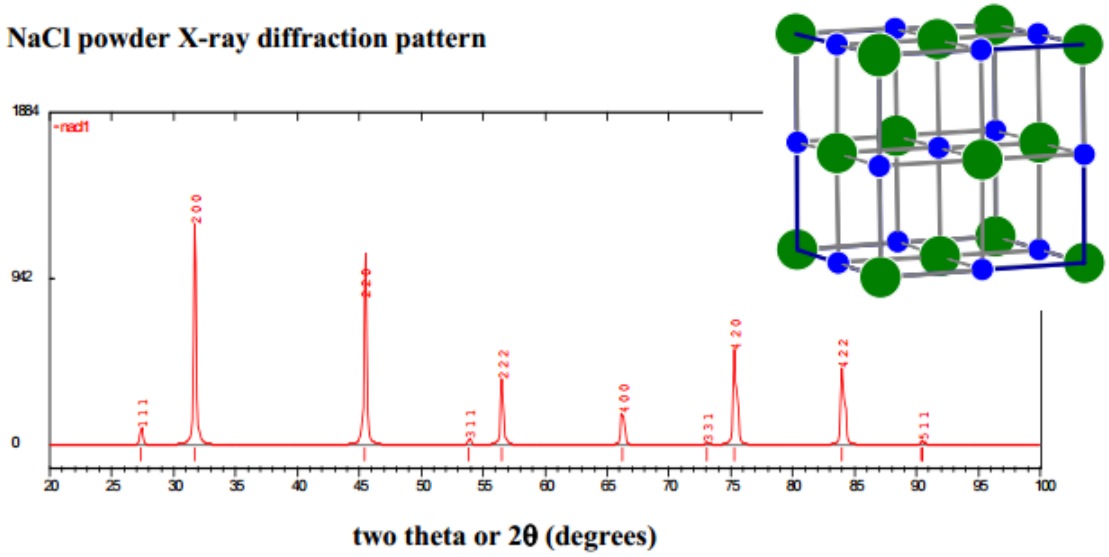

Figure 11: NaCl powder X-ray diffraction pattern.[35]

Powder X-ray diffraction is not commonly used for structure determination but is a powerful technique for phase characterization and identification. Comparison to databases of pure substances, like the International Centre for Diffraction Data's database,[36] can be used to determine the materials contained in an unknown mixture of materials.
Within a diffractogram, the value of 2θ can be used to determine the unit cell parameters, the intensity of the peaks can be used to determine the structure and for quantitative analysis and the peak width carries information about the crystallite size and micro-straining. Since amorphous materials do not have long-range order but might have local order, they affect the background of the diffractogram.

There are different geometries that can be used to obtain powder X-ray diffraction diffractograms. In this work, the PANanalytical X'PERT Pro X'Celerator powder diffractometer uses Bragg-Brentano geometry with a θ-θ configuration (Figure 12). In this geometry the sample is fixed and the source and detector move together to always be both at a θ angle with respect to the sample. In this way the detector is 2θ with respect to the incident beam, collecting the diffracted X-ray beam, following Bragg's law. Bragg-Brentano geometry can also be achieved

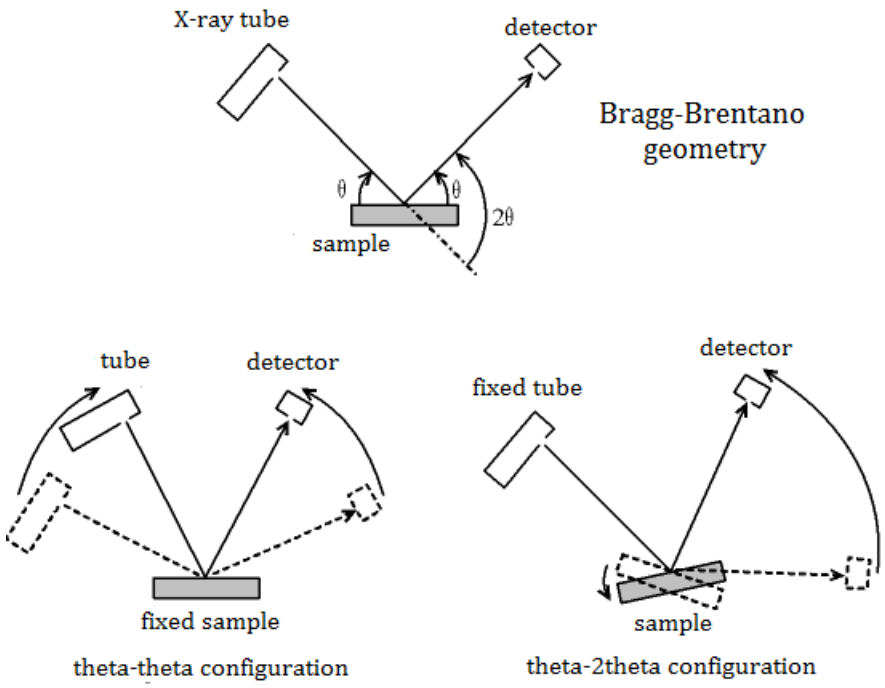

Figure 12: Bragg-Brentano geometry for X-ray powder diffraction. Top shows the relationship between the angles in this geometry. Below, the two possible configurations, where the sample is fixed and the X-ray tube is fixed, respectively.

by having a fixed source and have the sample and detector move, keeping the 2θ relationship between the 3 components.

1.4.3 Transmission Electron Microscopy

Transmission Electron Microscopy (TEM) is a technique where a beam of electrons pass through a very thin sample. The electron beam interacts with the sample as it goes through. This interaction is dependent on the atomic number of the elements present in the sample, heavier elements interact more often with the electrons and appear as dark shadows on a TEM image.

High-speed electrons from the electron beam can collide with inner shell electrons, which can cause the following phenomena: (1) a lower energy electron can be ejected (secondary electron); (2) the original electron is scattered (back-scattered electron); (3) an outer shell electron drops into the position formerly occupied by the ejected electron, from which an X-ray photon of the precise wavelength of the energy difference is emitted.

TEM detects the decrease in the electron beam caused by the first two phenomena. Scanning Electron Microscopy (SEM) detects the secondary and back-scattered electrons, while the analysis of the X-ray photon emitted is used in X-ray microanalysis.

Transmission electron microscopes are capable of higher resolution than optical microscopes due to their small deBroglie wavelength, when compared to visible light used in optical microscopes. Because of this, this technique is used to visualize objects of micro and nano-meter

scales.

The microscopes have 4 main parts (Figure 13). The electron gun is the source of electrons.

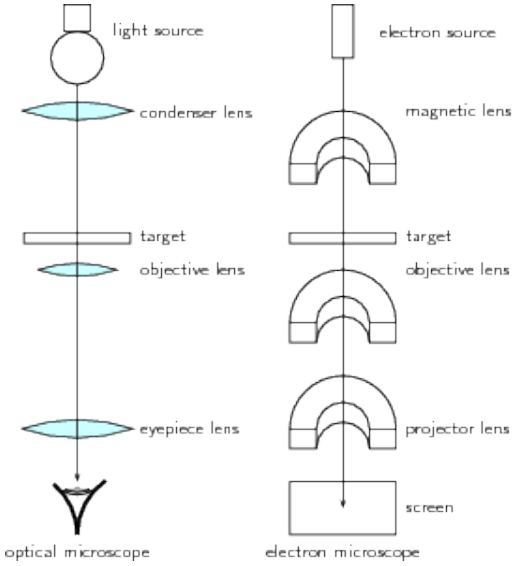

Figure 13: Comparison of an optical microscope with a transmission electron microscope.

It is usually composed of a tungsten filament that with a current passing through generates a flow of electrons. Secondly, a system of magnetic lenses (as opposed to optical lenses) focus the electron beam onto the target. The sample is usually prepared on a copper grid covered with a non-absorbing film. Finally the image is projected onto a phosphorescent viewing screen that glows when struck by electrons.[37]

2 Objective

9-HSA is known to be active against osteosarcoma.[3] The aim of this work is to functionalize hydroxyapatite (HA) with 9-HSA to obtain a bioactive material that combines the biocompatibility of HA toward bone with the cytostatic and/or cytotoxic properties of 9-HSA.

To achieve this objective, in this work potassium (9R)-9-hydroxystearate, the more water soluble salt of 9R-HSA, was synthesized from *Dimorphotheca sinuata* L. seeds and included in the direct synthesis of hydroxyapatite. The precursors and the novel materials were characterized by a series of techniques.

3 Experimental Methods

3.1 Materials

The *Dimorphotheca sinuata* L. seeds were bought from Galassi sementi SNC at Gambettola (FC, Italy). The reagents used, unless stated otherwise were acquired from Sigma-Aldrich (Milan). Flash chromatography was done with a silica gel (0.037-0.063 mm, Merck) stationary phase. Thin layer chromatography (TLC) was done with silica gel 60 from Fluka Analytical and the spots were revealed using an aqueous solution of $(NH_4)_6MoO_{24}$ (2.5%) and $(NH_4)_4Ce(SO_4)_4$ (4%) in 10% H_2SO_4.

For the hydrogenation reaction a Parr hydrogenator model 3911EKX is used with a hydrogen gas pressure of 40 psi.

3.2 Characterization

The nuclear magnetic resonance spectra (^{1}H, ^{13}C, DEPT) were obtained using Varian spectrometers Gemini 300, Mercury 400 and Inova 600 (Varian, Palo Alto). All spectra were obtained using either $CDCl_3$, DMSO-d_6 or D_2O as the solvent. The frequencies are given in Hz and the chemical shift δ in ppm using the chemical shift of $CHCl_3$ as the reference (δ = 7.26 ppm in ^{1}H-NMR and δ = 77.0 ppm in ^{13}C-NMR).

Gas chromatographic analyses were carried out with a Hewlett-Packard (HP) 5890 gas chromatograph directly interfaced with an Agilent 5970 mass selective detector. Injection temperature was 250°C (split injection mode split ratio 50:1) (HP-5MS column, 30 m, 0.25 mm, 0.25 μm film thickness). The oven temperature was programmed as follows: 60°C for 2 min, increased up to 260°C at the rate of 20°C/min, followed by 260°C for 20 min. The carrier gas was helium, used at a flow rate of 1 mL/min; the transfer line temperature was 280°C; the ionization was obtained by electron impact (EI), acquisition range was 50–500 m/z. EI mass spectra were recorded using a VG-7070E spectrometer at an ionization voltage of 70 eV. ESI-MS spectra were recorded on a WATERS 2Q 4000 instrument.

Fourier Transform Infrared (FT-IR) spectra of the organic compounds were recorded using a Perkin-Elmer FT-IR MOD 1600 spectrophotometer. FT-IR spectra of hydroxyapatite and 9R-HSA modified HA were recorded using a Bruker Alpha FT-IR in both ATR and transmission modes. For measurements taken in transmission mode the samples were prepared by grinding 1 mg of the material with 250 mg of potassium bromide and pressing the mixture into a pellet with a pressure of 10 tons per square inch during one minute.

Melting points were measured by a Büchi apparatus and were not corrected.

Thermogravimetric analysis was carried out using a Perkin Elmer TGA-7. Heating was performed in a platinum crucible in air flow (20 cm^3 min^{-1}) at a rate of 10°C min^{-1} up to 950°C. The samples weights were in the range 5–10 mg.

X-ray diffraction patterns were obtained using a PANanalytical X'PERT Pro X'Celerator

powder diffractometer using copper Kα characteristic radiation (λ = 1.5418 Å) and selected using a graphite monochromator, with a fixed divergent slit of $\frac{1}{4}^\circ$ and a fixed anti-scatter slit of $\frac{1}{2}^\circ$. Acquisitions were taken using three different scan programs: (1) Diffractograms obtained for crystalline phase identification were measured from 2θ =10° to 60° with 0.10° per step and a 0.128°/s scan rate. The analysis is qualitative and done by comparison to the diffractograms from the International Centre for Diffraction Data (ICDD) database.[36] (2) The cell parameters were determined using a lattice parameter refinement software called CELSIZ,[38] that uses the information from a series of reflections after the Miller indices have been attributed. The diffractograms for this determination are obtained from scans measured from 2θ =10° to 60° with 0.05° per step at a scan rate of 0.04°/s. Crystalline silicon was added as an internal standard and appears in the diffractograms as thin peaks at 28.443°, 47.304° and 56.122°. (3) Data was collected from all the samples relative to the 002 and 310 reflections for crystal size determination. The scan intervals chosen were 24.5°–27.5° and 38.0°–41.0°, for each reflection respectively. These were obtained with a step of 0.008° and a scan rate of 0.016°/s. The results were treated with the data treatment program MARQFIT[39] to obtain the half width at half maximum (HWHM). This value was corrected for instrumental broadening using the experimental value of the HWHM of silicon reflections ($\frac{1}{2}\beta_{Si} = 0.04^\circ$).

Transmission Electron Microscopy (TEM) was used to obtain information on crystal size and morphology. After being ground, hydroxyapatite crystals were dispersed in ethanol by ultrasound for 30 s. A drop of the suspension was added to the Formvar-covered copper grid and subsequently dried in air. The grid was analyzed using a Philips CM100 transmission electron microscope at 80 kV.

Contact angle measurements were done using a CAM 101 equipment. Pure HA and HSAHA were pelletized with 8 tons per square inch during two minutes. Pellets acted as the solid phase for the measurement, milliQ water was used as the liquid phase air as the third phase. Data was acquired with the KSV Contact Angle Measurement system software, by taking 3 frames per second during 30 s after the drop was set on the surface. Values obtained were an average of 5 drops.

Zeta potential measurements were done using Dynamic Light Scattering (Zetasizer Nano; Malvern Instruments). The samples were prepared by suspending 5 mg of powder 50 mL of MilliQ water after sonication for 2 minutes.

The specific surface area was measured using a Carlo Erba Sorpty 1750 BET analyzer using constant volume N_2 absorption with desorption at 80°C. All surface area measurements were obtained with 0.5 g of solid sample.

3.3 Synthesis of (9*R*)-9-hydroxyoctadecanoic acid

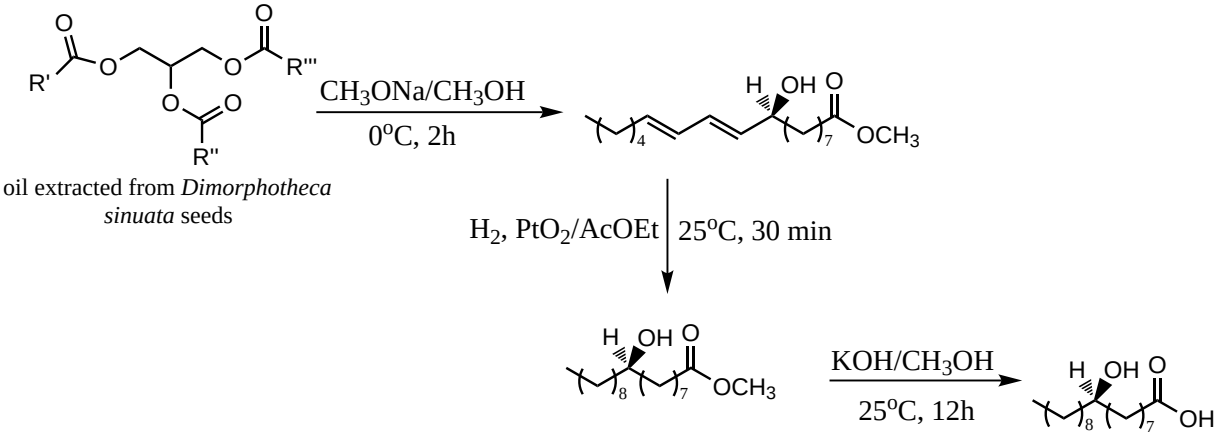

Figure 14: Scheme of the (9*R*)-9-hydroxystearic acid synthesis from *Dimorphotheca sinuata* L. seeds.

3.3.1 Extraction of oil from *Dimorphotheca sinuata* L. seeds

12 g of *Dimorphotheca sinuata* L. seeds were ground and added to a three-necked round-bottom flask and stirred under nitrogen with 210 mL of $CHCl_3$/MeOH (2:1) for 24h. This suspension was filtered under vacuum and washed with $CHCl_3$ (3 x 20 mL). The solution was acidified with 20 mL of 0.1 M HCl and 0.1 M NaCl aqueous solution and then extracted with $CHCl_3$ (3 x 15 mL). The organic layers were combined and dried over anhydrous $MgSO_4$. After filtration, the yellow solution was dried *in vacuo* at 30°C to obtain 4.0 g of yellow oil.

3.3.2 Transesterification of the oil from *Dimorphotheca sinuata* L.

The yellow oil was dissolved in 40 mL MeOH and treated with 1 M (2.16 g) of $NaOCH_3$ and stirred under N_2 atmosphere at 0°C for 2h. The resulting solution was acidified to pH 5.0 (presents color change from green to yellow) and extracted with n-hexane (3 x 20 mL). The hexane layers were combined and dried over anhydrous $MgSO_4$ and, after filtration, the solvent was removed under reduced pressure to give 2.2 g of oil.

3.3.3 Hydrogenation of the esterified oil

The bright yellow oil was dissolved in 10 mL of ethyl acetate and transferred to a 500 mL reaction bottle with a catalytic amount of PtO_2 (Adam's catalyst). This mixture was subjected to hydrogenation in a Parr apparatus with 40 psi H_2 pressure for 35 min. The resulting solution was filtered over celite and the solution concentrated under vacuum. A ^{1}H NMR spectrum is obtained to confirm the absence of vinylic hydrogens before proceeding.
Flash chromatography (petroleum ether / diethyl ether 7:3) of the residue gave methyl (9R)-9-hydroxyoctadecanoate as a white solid (0.743g). (m.p.: 50-51.2°C)

^{1}H NMR (399.9 MHz, $CDCl_3$, TMS): 3.65 (s, 3H, OCH_3), 3.60-3.55 (m, 1H, C<u>H</u>OH), 2.29 (t, 2H, J = 7.6 Hz, CH_2COO), 1.61 (quint, 2H, J = 7.4 Hz, C<u>*H*</u>$_2CH_2COO$), 1.50-1.20 (m, 27H, incl. OH), 0.87 (t, 3H, J = 7.0 Hz, CH_3).
^{13}C NMR (100.6 MHz, $CDCl_3$): 174.1, 71.7, 51.3, 37.4, 37.3, 33.9, 31.8, 29.6, 29.56, 29.5, 29.4, 29.2, 29.1, 28.9, 25.5, 25.4, 24.8, 22.6, 14.05.
The attribution of the ^{13}C NMR signals are reported in Annex B.
IR($CHCl_3$): 3427, 1728 cm^{-1}.

3.3.4 Hydrolysis of methyl (9*R*)-9-hydroxyoctadecanoate

To obtain (9*R*)-9-hydroxyoctadecanoic acid 0.300 g of methyl (9*R*)-9-hydroxyoctadecanoate was stirred in 20 mL of a 10% w/v methanolic solution of KOH for 12h at room temperature. The reaction was monitored by TLC. The solvent was removed under vacuum and the light yellow solid was dissolved in water and acidified until precipitation. This mixture was extracted with ethyl acetate and after this was dried with anhydrous $MgSO_4$ and, after filtration, the solvent was removed under vacuum. (9*R*)-9-hydroxyoctadecanoic acid (9R-HSA) was then re-crystallized from methanol to give 0.232 g of white acicular crystals. (m.p. 74.5-78.2°C from methanol, literature:[40] 76-77°C) ^{1}H NMR (399.9 MHz, $CDCl_3$, TMS): 4.73 (broad s, 1H, OH), 3.53-3.63 (m, 1H, C<u>H</u>OH), 2.34 (t, 2H, J = 7.4 Hz, CH_2COO), 1.63 (quint, 2H, J = 7.1 Hz, C<u>*H*</u>$_2CH_2COO$), 1.49-1.16 (m, 27H, incl. OH), 0.88 (t, 3H, J = 7.0 Hz, CH_3).
^{13}C NMR (100.6 MHz, $CDCl_3$, TMS): 178.7, 72.0, 37.5, 37.4 33.5, 31.9, 29.7, 29.6 (two overlapped signals), 29.4, 29.3, 29.2, 29.0, 25.7, 25.5, 24.7, 22.7, 14.1.

3.3.5 Synthesis of the potassium (9*R*)-9-hydroxyoctadecanoate

2.022 g of 9R-HSA was dissolved in a equimolar KOH/methanol 5% solution and left stirring for 3h. The reaction was monitored by TLC and once completed the methanol was dried under vacuum. The resulting light yellow solid was dissolved in 10 mL of boiling water, left to cool to room temperature, finally, the precipitate was filtered and removed, the resulting mother liquor was dried under vacuum at 45°C. 1.561 g of potassium(9R)-9-hydroxyoctadecanoate were obtained as a light yellow powder from the mother liquor.

3.4 Derivatization of 9-HSA with (*R*)-(-)-O-acetylmandelic acid

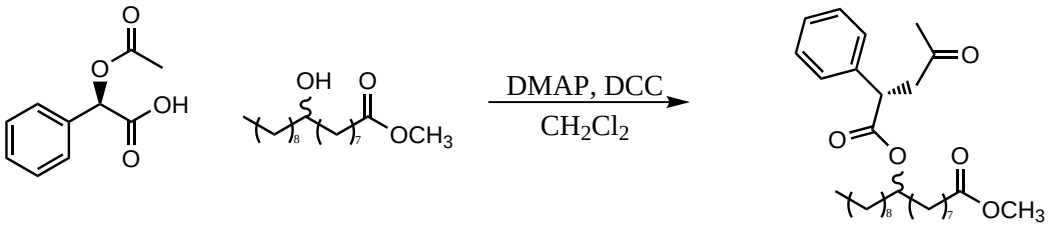

The optical purity of methyl (9*R*)-9-hydroxyoctadecanoate was determined by ^{1}H NMR analysis after derivatization with (*R*)-(–)-O-acetylmandelic acid using the following procedure: 0.010 g of (*R*)-(–)-O-acetylmandelic acid and 0.002 g of DMAP were dissolved, under nitrogen gas, in 300 μL of anhydrous CH_2Cl_2 and stirred at 0°C (ice-bath). To this solution, a solution of 0.008 g of methyl (*R*)-9-hydroxystearate and 0.010 g of DCC in 500 μL of anhydrous CH_2Cl_2 was added. After a few minutes a white solid precipitated and the reaction was monitored by TLC (eluent: n-hexane – AcOEt 3:1) until it resulted complete. The product was purified by preparative TLC (eluent: n-hexane – AcOEt 3:1) and the spot with RF 0.6 was scraped. The product was dissolved in methanol and the suspension was filtered. After removal of the solvent, the product was dissolved in $CDCl_3$ and ^{1}H NMR spectroscopy at 600 MHz showed only one signal corresponding to H-2 signal of the mandelic moiety (on the racemic mixture the signals of H-2 of the mandelic moiety, as well as those of OCH_3 signals of the ester moiety, resulted to be satisfactorily separated). The same observation was made by ^{1}H NMR analysis of the crude reaction mixture prior its purification by preparative TLC.

The spectra of the diastereotopic products have been reported[4] and present the following peaks:

Methyl (9*R*)-9-[(2*R*)-2-(acetyloxy)-2-phenylacetyl]oxyoctadecanoate: ^{1}H NMR (599.7 MHz, $CDCl_3$): 7.51-7.44 (m, 2H, phenyl), 7.40-7.34 (m, 3H, phenyl), 5.874 (s, 1H, H-2), 4.88 (quint, 1 H, J = 6.36 Hz, H-9), 3.671 (s, 3H, OCH_3), 2.30 (t, 2H, J = 7.55 Hz, CH_2CO), 2.19 (s, 3H, $OCOCH_3$), 1.68-1.00 (m, 28 H, CH_2), 0.89 (t, 3H, J = 6.8 Hz, CH_3).

Methyl (9*S*)-9-[(2*R*)-2-(acetyloxy)-2-phenylacetyl]oxyoctadecanoate: ^{1}H NMR (599.7 MHz, $CDCl_3$): 7.51-7.47 (m, 2H, phenyl), 7.42-7.37 (m, 3H, phenyl), 5.870 (s, 1H, H-2), 4.86 (quint, 1 H, J = 6.36 Hz, H-9), 3.667 (s, 3H, OCH_3), 2.27 (t, 2H, J = 7.55 Hz, 2H, CH_2CO), 2.19 (s, 3 H, $OCOCH_3$), 1.68-1.00 (m, 28H, CH_2), 0.88 (t, 3H, J = 6.9 Hz, CH_3).

The ^{1}H NMR spectroscopy at 600 MHz showed two signals at 3.670 and 3.666 ppm corresponding to the R and S derivatives of methyl 9-hydroxystearate respectively with a ratio of 9 to 1, indicating an enantiomeric ratio of about 90:10 of methyl (9*R*)-9-hydroxystearate. This ratio was confirmed also by considering another diagnostic signal, i.e. that belonging to the H-2 proton of the mandelic moiety of the HSA derivative. Also for this signal there is a detectable chemical shift difference between the two diastereomers (5.868 and 5.872 ppm for *R*-9 and *S*-9 derivative, respectively). The presence of two diastereoisomers might be due to the derivatization method and therefore other methods are currently being tested.

3.5 Synthesis of crystalline hydroxyapatite

3.5.1 Preparation of decarbonated water

2 L of distilled water are heated in a round bottom flask with a condenser under nitrogen. The water is refluxed during one hour and cooled under nitrogen in an ice bath. It can then be transferred into flasks previously purged with nitrogen and should be used within 5 days.

3.5.2 Hydroxyapatite synthesis

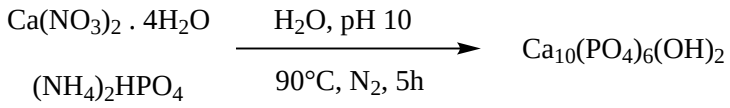

In a 500 mL three-necked round-bottom flask 50 mL of 0.64 M diammonium hydrogen phosphate (4.29 g in decarbonated water) was heated with magnetic stirring with a condenser under nitrogen to 90°C. Once the temperature is reached, 25% ammonia solution is added to adjust the pH to 10. To this flask 50 mL of 1.08 M calcium nitrate tetrahydrate (12.75 g in decarbonated water), also adjusted to pH 10 with a 25% ammonia solution, was added slowly at a rate of approximately 3 mL/min. Once the addition was finished, ammonia is added to adjust the pH to 10. The reaction is kept under heating for 5 h, periodically verifying the temperature and pH and adjusting as necessary. Once completed it is cooled under nitrogen gas then washed three times with 90 mL decarbonated water, each time centrifuging at 10000 rpm for 10 min. Finally, the white powder was dried overnight at 37°C.

3.6 Synthesis of (9*R*)-9-hydroxystearic acid modified hydroxyapatite

The synthesis of 9HSA-modified hydroxyapatite is done with the same method as the synthesis of HA with the inclusion of 5 , 10, 15 and 20 mmol.L^{-1} of potassium (9*R*)-9-hydroxystearate (Table 1). Each concentration was done in duplicate. The solid was added to the round-bottom flask prior to the addition of calcium nitrate tetrahydrate and mixed and heated until the solution was homogeneous. The addition of calcium nitrate started only after the complete dissolution of 9R-HSA-K.

Table 1: Samples subjected to absorption of potassium (9R)-9-hydroxystearate.

Sample	Amount of 9R-HSA-K (mg)	[9R-HSA] (10^{-3} mol.L^{-1})
HSAHA 5	170	5
HSAHA 10	340	10
HSAHA 15	510	15
HSAHA 20	680	20

4 Results and Discussion

4.1 Synthesis of methyl (9*R*)-9-hydroxystearate

(9R)-9-hydroxystearic acid was obtained by hydrogenation of dimorphecolic acid isolated from *Dimorphotheca sinuata* L. seeds. This procedure was chosen because of the interest in the enantiomerically pure (9R)-9-hydroxystearic acid due to its increased HDAC1 activity when compared to the S-enantiomer in simulations[9] and in cells.[4]

To obtain 9R-HSA the triglycerides were extracted from *Dimorphotheca sinuata* L. seeds then transmethylated, both under nitrogen gas to avoid eventual oxidation of the double bonds in dimorphecolic acid. For sake of clarity Figure 14, already reported in the experimental part, is reported again in this section. Successively, the mixture containing several fatty acid esters from the seeds is hydrogenated in a Parr apparatus using PtO_2 as a heterogeneous catalyst. This reaction was also tested with 10% carbon-supported palladium (Pd/C) as an attempt to check if the reduction step can affect the configuration of the C-9 nevertheless this reaction presented lower yield with similar enantiopurity of the final product. At this step a ^{1}H-NMR spectrum is obtained to verify if the hydrogenation is complete. This is done by seeing that there are no more vinylic hydrogens in the 5-6 ppm region. Once the reaction completion is confirmed the fatty acid esters are separated by flash chromatography and only methyl (9R)-9-hydroxystearate is kept.

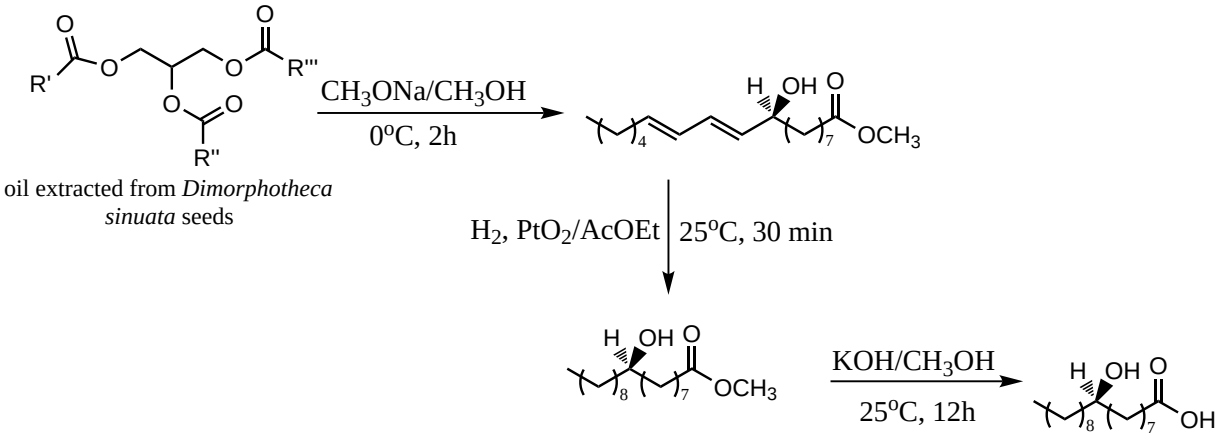

Figure 14: Scheme of the (9*R*)-9-hydroxystearic acid synthesis from *Dimorphotheca sinuata* L. seeds.

4.1.1 Nuclear Magnetic Resonance Spectrometry

The resulting ^{1}H-NMR spectrum of methyl (9R)-9-hydroxystearate is shown in Figure 15. In

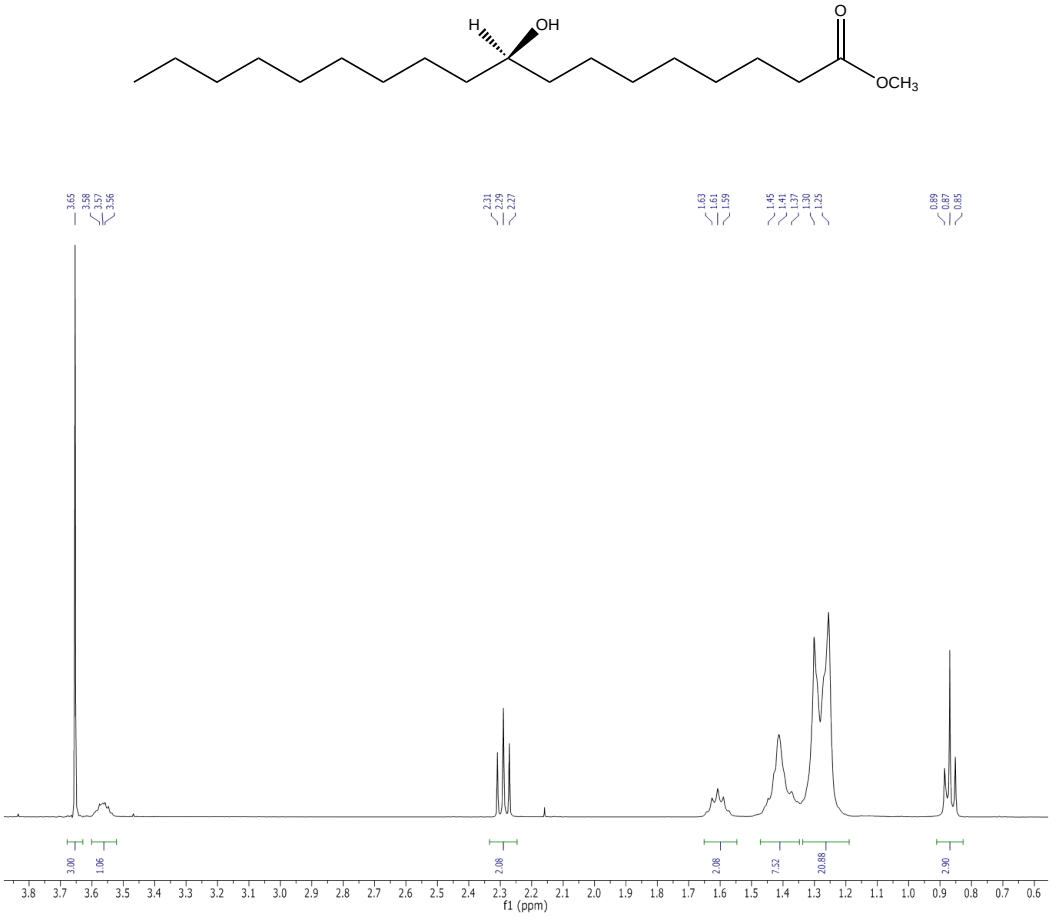

Figure 15: ^{1}H-NMR spectrum of methyl (9R)-9-hydroxystearate.

this spectrum the most notable peak is the intense singlet at 3.65 ppm that integrates for 3H and is attributed to the ester methoxy hydrogens. The presence of the close electronegative oxygen is what make this signal the most deshielded on the spectrum. Beside this peak, a broad multiplet between 3.63 and 3.53 ppm is seen. This integrates for 1H and is attributed to the hydrogen on the same carbon as the hydroxyl group, which is why it is so deshielded as well. The splitting is not very well defined at this field strength but is expected to be *dddd* because all the hydrogens 3 bonds away from it form two diastereotopic pairs. At 2.29 ppm there is a triplet that integrates for 2H. This chemical shift is expected for a pair of hydrogens beside an ester carbonyl, much less deshielded than the methoxyl group, but more than a typical aliphatic chain. At 1.61 ppm there is a quintet that is most likely on the β-carbon from the carbonyl. It is actually a *dddd* since all hydrogens are diastereotopic but it appears as a quintet because the J-coupling values are so similar. Unfortunately, between 1.50 and 1.20 ppm the bulk of the hydrogens are found but the overlapping at this field does not allow to distinguish them. Here are all 27 remaining hydrogens, including that of the hydroxyl group. Finally, at 0.87 ppm, the most shielded peak with an integration of 3H is the methyl group at the end of the

long aliphatic chain and appears as a triplet because the two diastereotopic hydrogens on the neighboring carbon both cause the same J-splitting.

4.1.2 Mass Spectrometry

The mass spectrum of methyl (9*R*)-9-hydroxystearate (Figures 16, 17 and 18) was obtained by electron impact (EI-MS). The molecular ion is not present in this spectra. We do see the typical M^+-31 at m/z = 283, the release of a methoxy radical, characteristic of a methyl ester. The base peak in this spectrum is m/z = 155, the breaking of a aliphatic bond α to the hydroxyl group on carbon 9. This is proof that the acid is indeed methyl 9-hydroxystearate and not another methyl hydroxystearate.

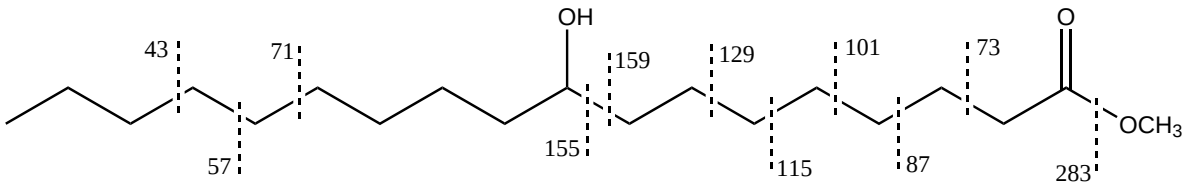

Figure 16: Main cleavage positions seen on the mass spectrum of methyl 9-hydroxystearate.

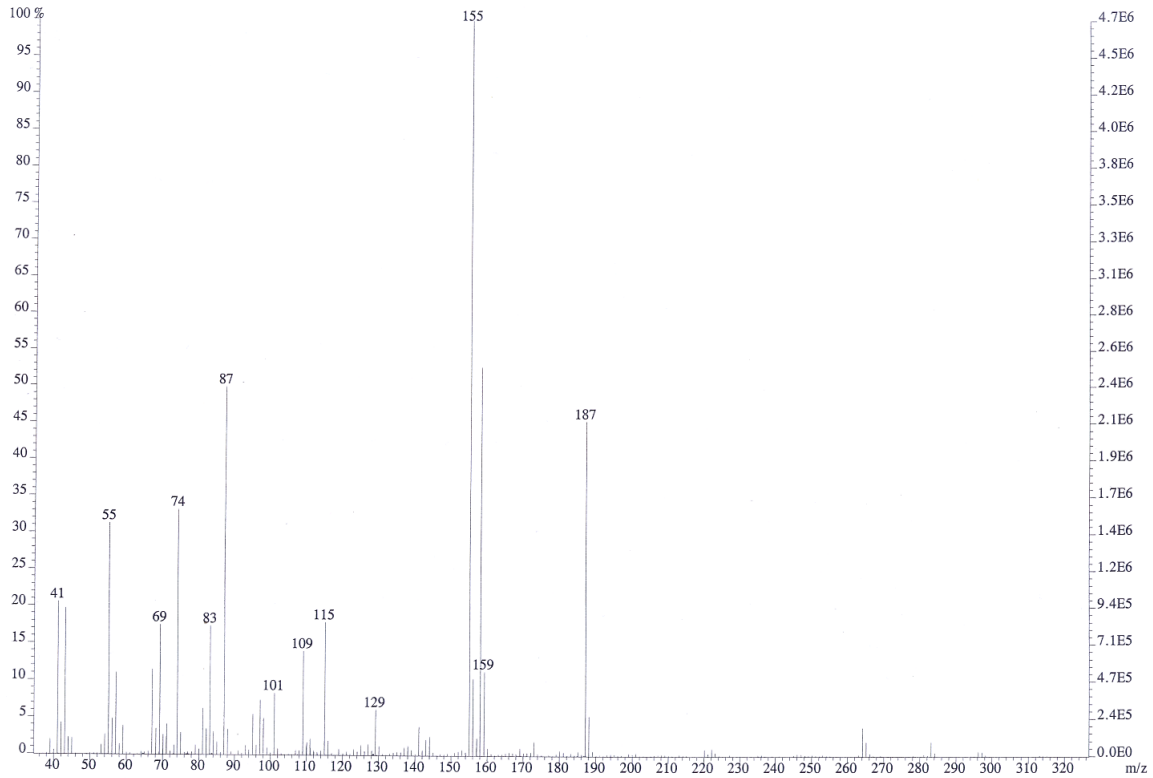

Figure 17: Electron Impact Mass Spectrum of methyl 9-hydroxystearate.

Other visible peaks in this mass spectra include the cleavage of the aliphatic chain after the hydroxyl group with the charge remaining on the smaller fragment (m/z = 43, 57), sometimes forming the C_nH_{2n-1} fragment (m/z = 41, 55, 69, 83)[41] and of the chain between the carbonyl

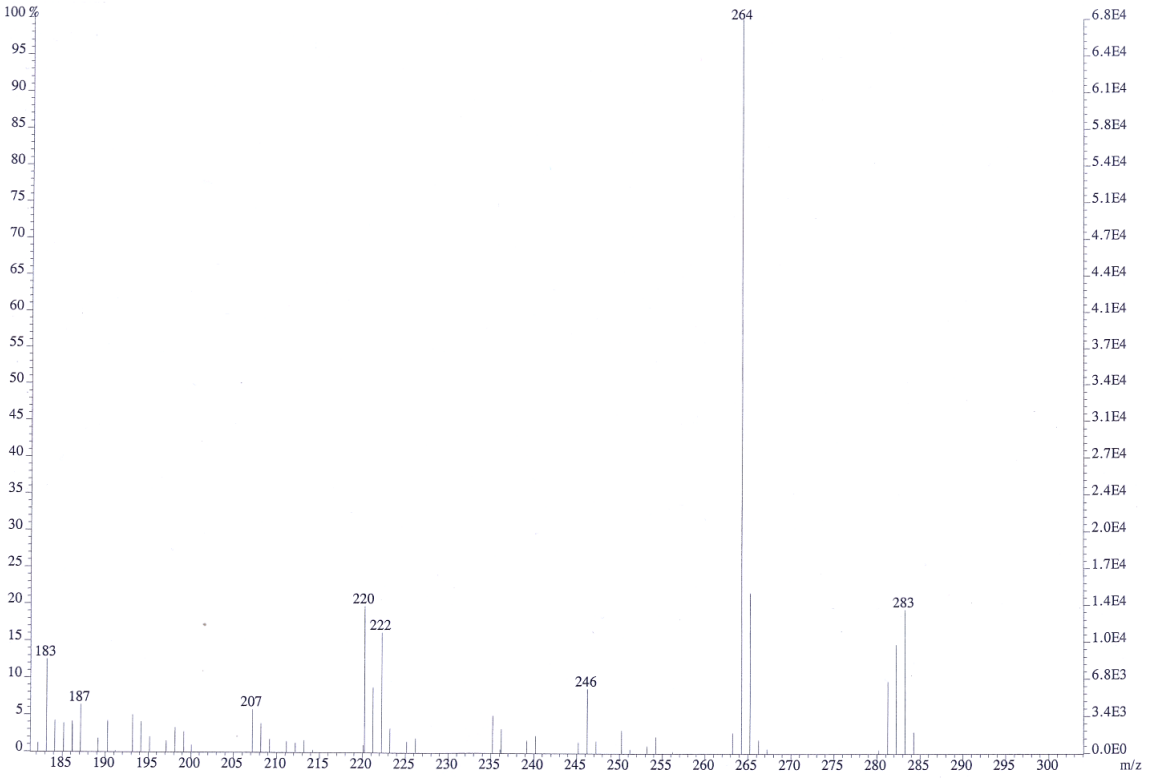

Figure 18: Enlargement of the Mass Spectrum of methyl 9-hydroxystearate near the molecular ion.

and the chiral center (m/z = 73, 87, 101, 115, 129, 159). We see the peak corresponding to a sequential rearrangement that results in the loss of water and methanol (m/z = 264) and an intense peak when the chain breaks on the other bond α to the hydroxyl at m/z = 187. The rearrangement that releases 1-nonanol (m/z = 158) is also a very intense peak.

4.2 Derivatization of 9-HSA with (*R*)-(-)-O-acetylmandelic acid

The enantiomeric purity of the methyl ester of 9-HSA was determined by derivatization using (*R*)-(-)-O-acetyl mandelic acid because due to its high symmetry, methyl (9*R*)-9-hydroxystearate is only slightly levorotatory ($[\alpha_D^{25}]$= -0.18°, c 10.0, ethanol)[42] making determining the enantiomeric ratio by optical methods difficult. The reaction used is a soft method for acylating alcohols[43] and has been used for separating alcohol enantiomers for over 30 years.[44] This reaction was done with methyl (9*R*)-9-hydroxystearate instead of (9*R*)-9-hydroxystearic acid because there would be competing reactions in the mixture. DCC in the presence of a catalytic amount of DMAP would cause the hydroxyl group to attack all acids in solution, both the desired (*R*)-(-)-O-acetyl mandelic acid and other 9R-HSA molecules resulting in an even more complex mixture of products.

Figure 20 shows the two peaks found in the spectrum that correspond to the methoxy hydrogens in both (*R*)-methyl 9-((*R*)-2-acetoxy-2-phenylacetoxy)octadecanoate and (*S*)-methyl 9-((*R*)-2-acetoxy-2-phenylacetoxy)octadecanoate (Figure 19) and by comparing their areas the

enantiomeric ratio was found to be approximately 90:10 for the R-enantiomer of methyl (9R)-9-hydroxystearate. The rest of the spectrum is not shown and interpreted because the NMR tube contains the whole of the reaction medium including excess reagents used in the reaction. Purification is not necessary to reach the necessary information, also, during the purification by flash chromatography some amount of one of the two diastereoisomers might not be completely collected, thus giving an erroneous result.

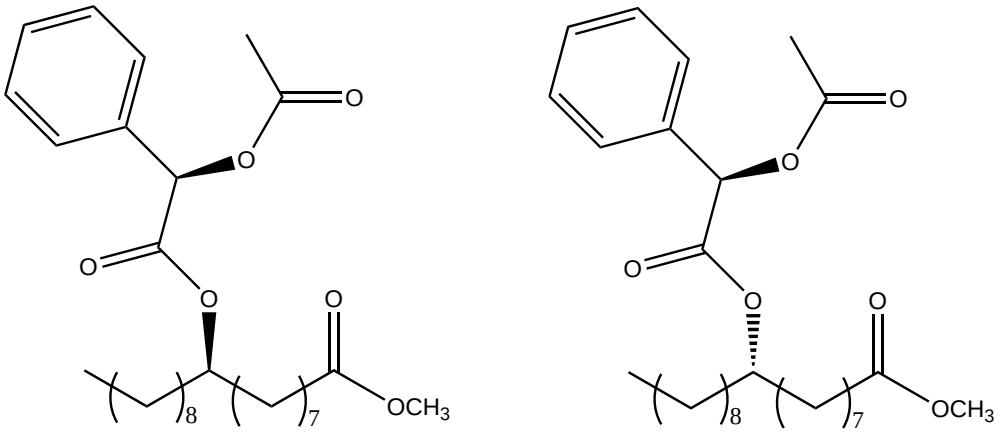

(R)-methyl 9-((R)-2-acetoxy-2-phenylacetoxy)octadecanoate

(S)-methyl 9-((R)-2-acetoxy-2-phenylacetoxy)octadecanoate

Figure 19: Diastereoisomers formed in the derivatization of 9-HSA with (R)-(-)-O-acetyl mandelic acid.

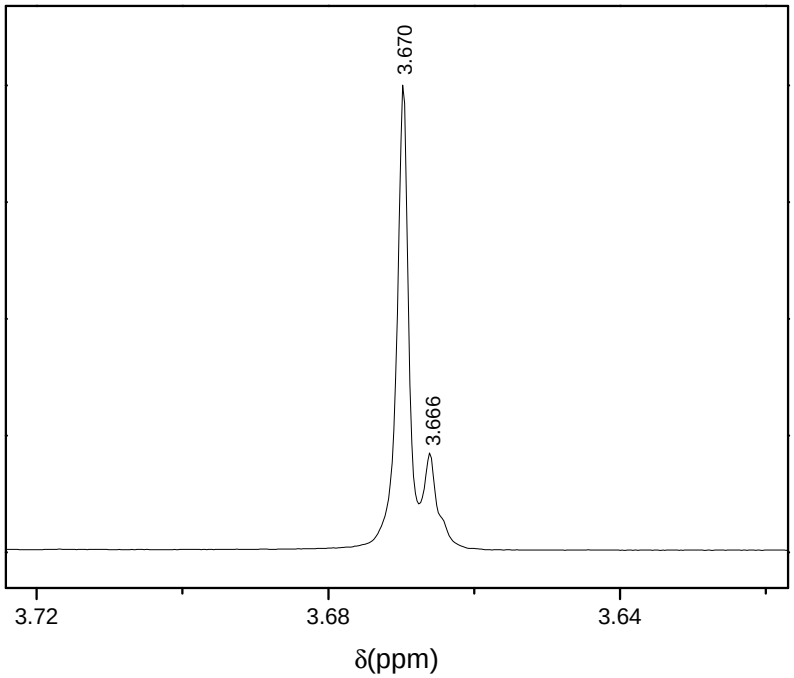

Figure 20: Enlargement of the NMR spectrum of 9-HSA derived with (R)-(-)-O-acetylmandelic acid showing the ester methoxyl hydrogens of both diastereoisomers.

4.3 Synthesis of (9*R*)-9-hydroxystearic acid

9R-HSA is produced by converting the methyl ester into the potassium salt by reacting it with a large excess of potassium hydroxide in methanol. This reaction can be accompanied by TLC where the methyl ester will disappear but the potassium salt does not run in organic solvents. Once complete, which can take as little as 3 h or as much as 12 h, the reaction is acidified and some precipitation can be seen. This is extracted in ethyl acetate and isolated.

4.3.1 Nuclear Magnetic Resonance

The resulting ^{1}H-NMR spectrum is shown in Figure 21. The attribution of the NMR spectrum of 9R-HSA is very similar to that of the methyl ester. The main differences are the absence of the methoxy group and the appearance of an acid OH broad peak at 4.73 ppm but whose exact position varies from one experiment to another. All other peaks were attributed like the methyl ester and did not show significant changes in the chemical shift.

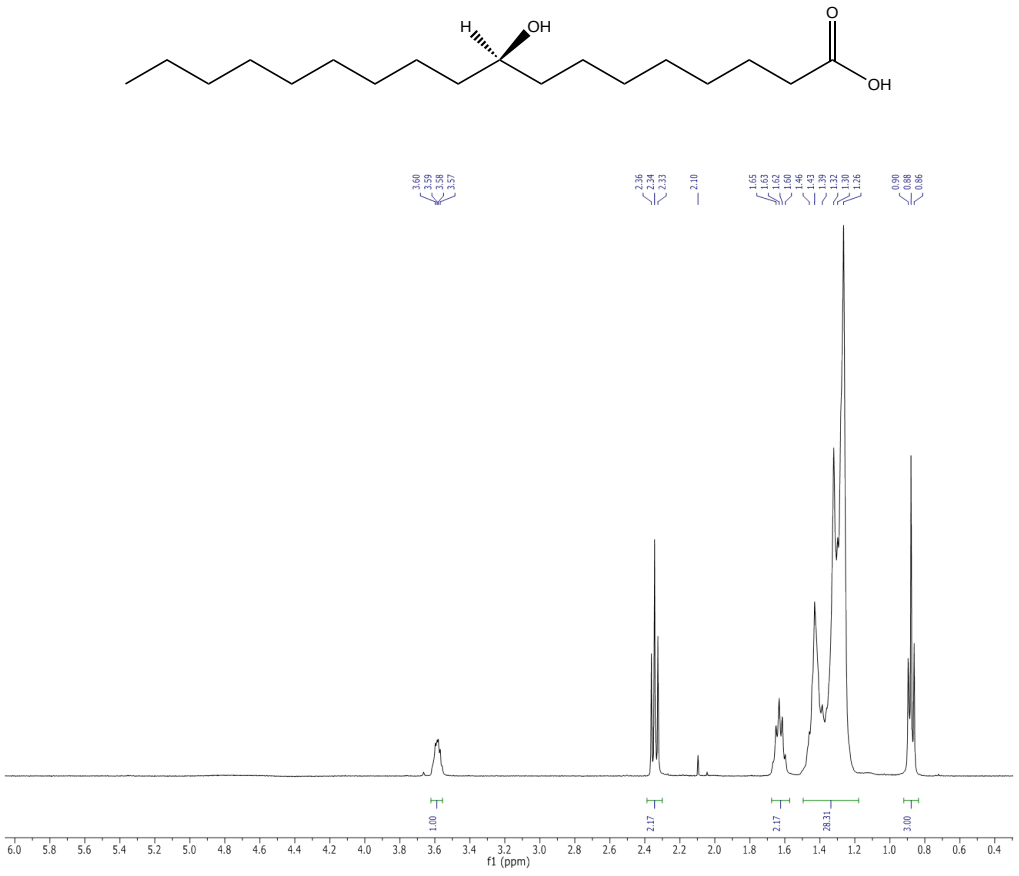

Figure 21: ^{1}H-NMR spectrum of (9*R*)-9-hydroxystearic acid.

4.3.2 Thermogravimetric Analysis

For comparison reasons, 9R-HSA was analyzed by thermogravimetric analysis (Figure 22). It showed complete decomposition of the acid before 600°C.

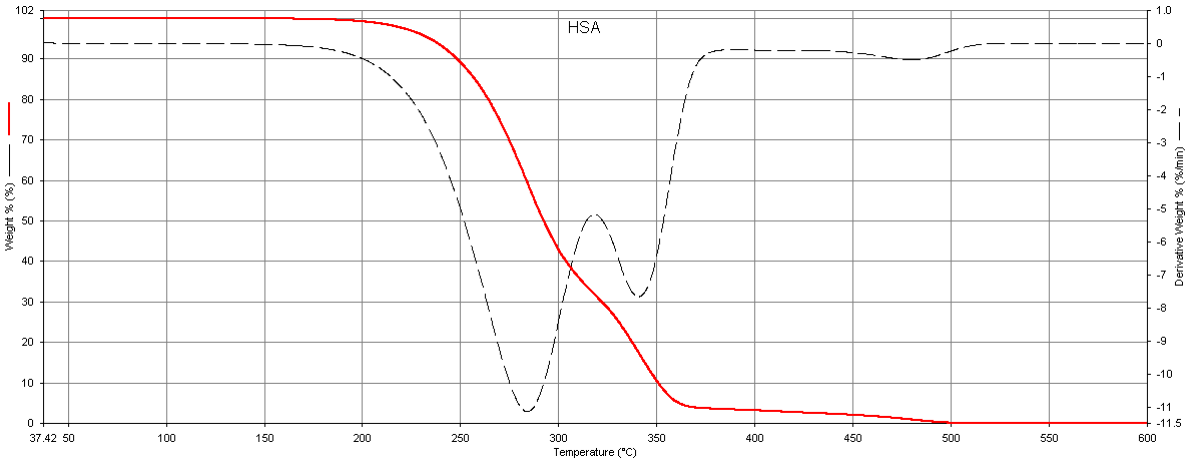

Figure 22: Thermogravimetric analysis of (9R)-9-hydroxystearic acid.

4.3.3 Mass Spectrometry

The mass spectrum of (9R)-9-hydroxystearic acid (Figures 24 and 25) was obtained by electron impact (EI-MS). The molecular ion is not present in this spectra, as is expected for a long-chain carboxylic acid. We do see the typical M^+-17 at m/z = 283, the loss of the terminal OH, characteristic of a carboxylic acid. The base peak in this spectrum is m/z = 155, the breaking of a aliphatic bond α to the hydroxyl group on C-9. This is proof that the acid is indeed 9-hydroxystearic acid and not another hydroxystearic acid. Other visible peaks (Figure 24)

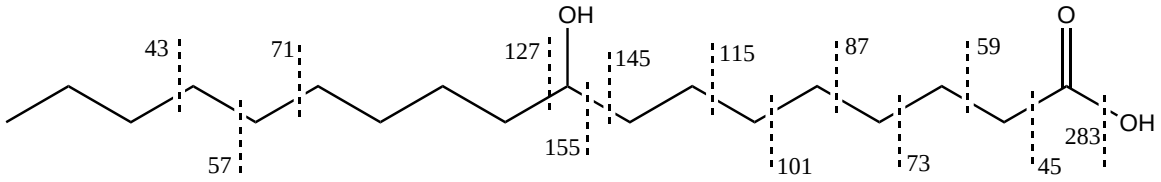

Figure 23: Main cleavage positions seen on the mass spectrum of 9-hydroxystearic acid.

in this mass spectra include the cleavage of the aliphatic chain after the hydroxyl group with the charge remaining on the smaller fragment (m/z = 43, 57, 71, 99, 127), sometimes forming the C_nH_{2n-1} fragment (m/z = 41, 55, 69, 83, 97)[41] and of the chain between the carbonyl and the chiral center (m/z = 45, 59, 73, 87, 101, 115). We also see a peak caused by two sequential loses of water at m/z = 264. The rearrangement that releases 1-nonanol appears at m/z = 144.

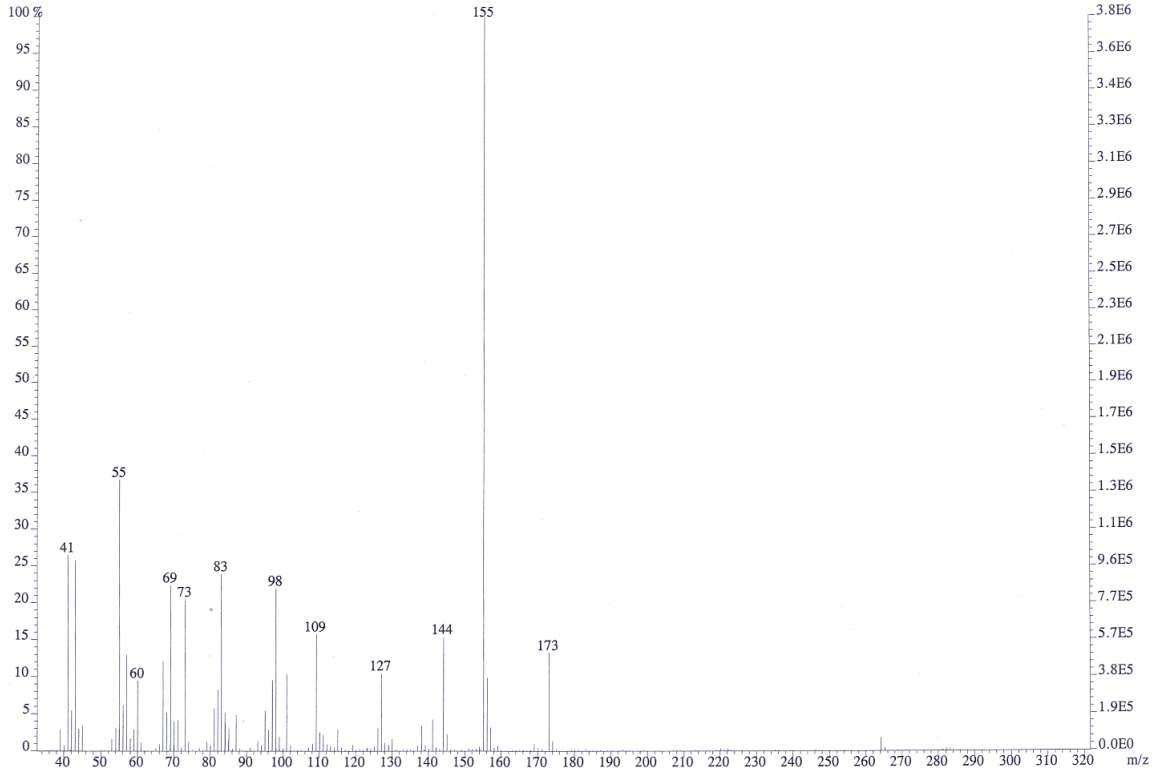

Figure 24: Electron impact mass spectrum of 9-hydroxystearic acid.

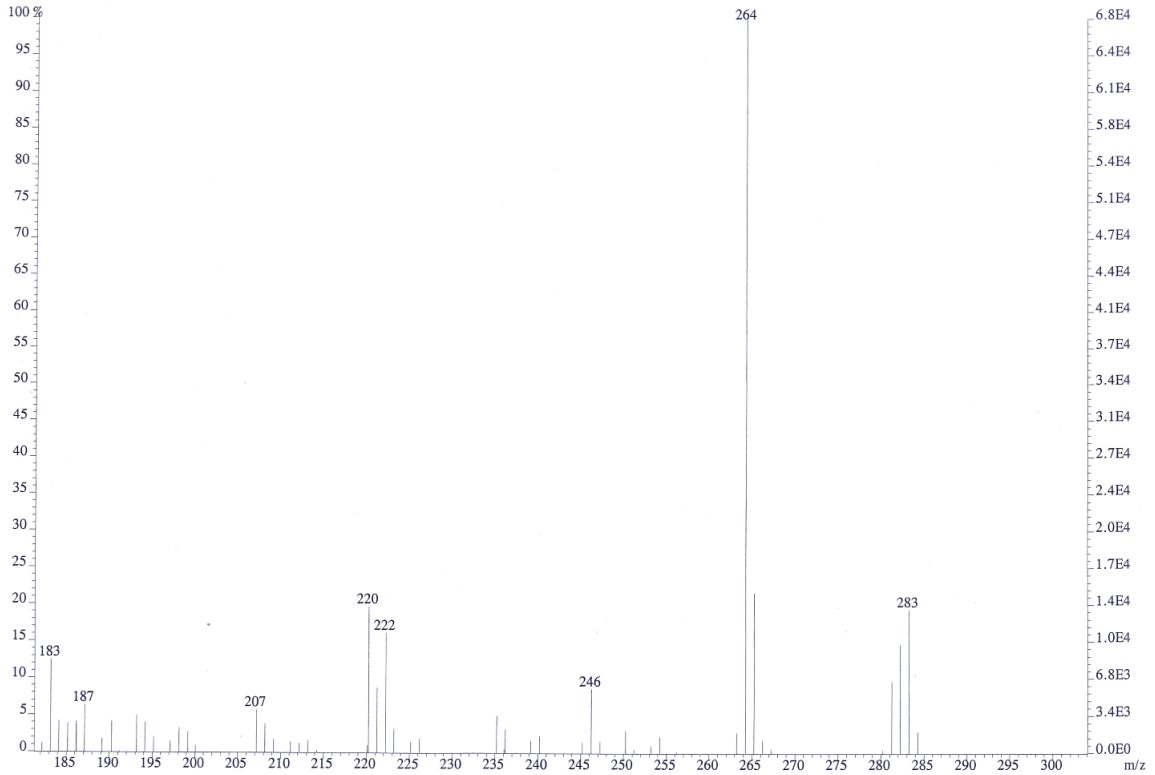

Figure 25: Enlargement of the Mass Spectrum of 9-hydroxystearic acid around the molecular ion.

4.4 Synthesis of potassium (9*R*)-9-hydroxystearate

To include 9R-HSA in the synthesis of hydroxyapatite it needed to be water soluble. As expected from an 18-carbon chain fatty acid, it was not soluble in its acid form therefore several salts

of 9R-HSA were prepared using stoichiometric quantities of the metal hydroxide in methanol, isolated as solids and tested towards their solubility in water. Sodium (9R)-9-hydroxystearate proved to be a particularly insoluble salt, not dissolving readily in any pure solvent, only a small amount was dissolved in dimethyl sulfoxide (DMSO-d_6) to obtain an NMR spectrum and confirm its purity. Both the potassium and ammonium salts of 9R-HSA proved to be more readily dissolved in water, especially once heated above 85°C. Since potassium (9R)-9-hydroxystearate (9R-HSA-K) was the more water soluble of the two it was chosen to be used in the HA synthesis.

4.4.1 Nuclear Magnetic Resonance

Due to solubility the ^{1}H NMR spectrum of potassium (9R)-9-hydroxystearate the spectrum was obtained in D_2O instead of $CDCl_3$ (Figure 26). The attribution of this spectrum is analogous to (9R)-9-hydroxystearic acid without the presence of the broad hydroxyl proton resonance.

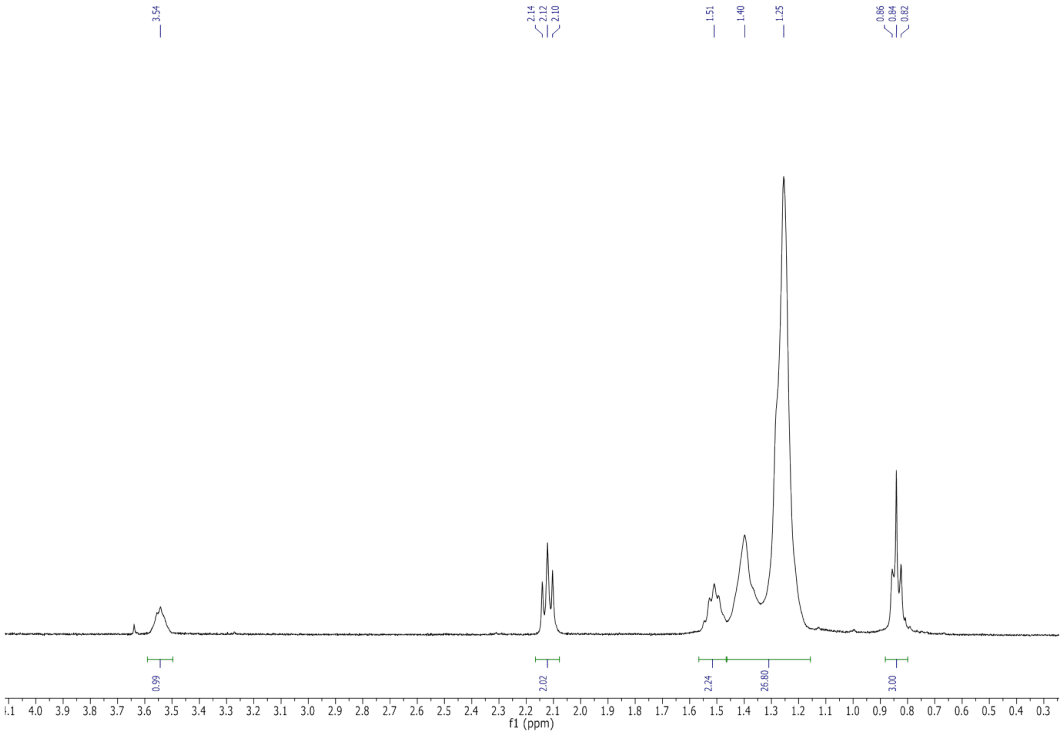

Figure 26: ^{1}H-NMR spectrum of potassium (9R)-9-hydroxystearate.

4.4.2 Mass Spectrometry

The mass spectrum of potassium (9R)-9-hydroxystearate was obtained using Electron Spray Ionization (ESI) mass spectrometry because this technique is a soft ionization technique which permits the visualization of the molecular ion, which cannot be seen under harsher ionization conditions. The negative mode was used to observe the presence of the organic anion. The main peak at m/z = 299 is the conjugate base of 9R-HSA. The smaller peak at m/z = 149 represents the double salt, a doubly deprotonated form of 9R-HSA.

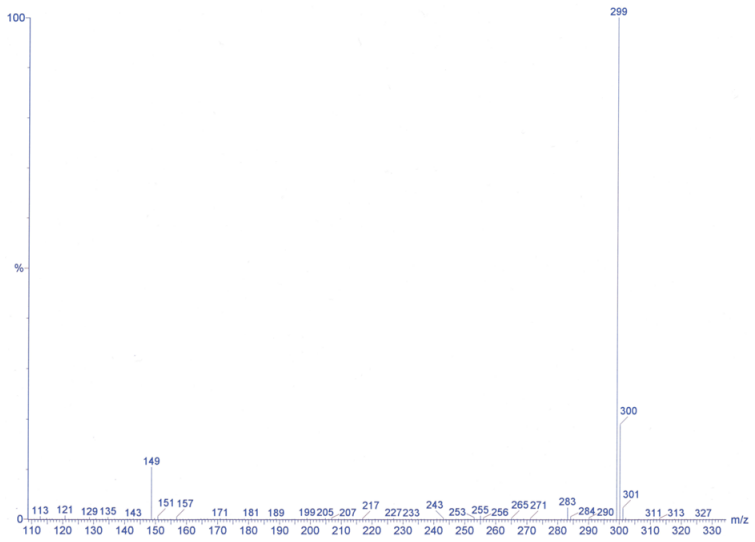

Figure 27: ESI Mass spectrum obtained for potassium (9*R*)-9-hydroxystearate.

4.5 Synthesis of crystalline hydroxyapatite

Crystalline hydroxyapatite (HA) was synthesized by precipitation in a basic aqueous solution using $Ca(NO_3) \cdot 4\,H_2O$ and $(NH_4)_2HPO_4$. The choice of calcium nitrate over calcium chloride was shown to produce more a more crystalline product and avoid chloride incorporation in the crystal structure.[13] Hydroxyapatite was prepared by the slow addition of $(NH_4)_2HPO_4$ onto $Ca(NO_3)_2 \cdot 4\,H_2O$. This produced 5.46 g of hydroxyapatite as a white powder with a yield of 98%.

4.5.1 Fourier-transform infrared spectrum

The experimental transmission Fourier-transform infrared (FT-IR) spectrum of hydroxyapatite is shown in Figure 29. It shows the characteristic infrared resonances pertaining to HA, as summarized in Table 2 (*vide infra*). One of the main absorption bands of HA is the thin band at 3569 cm^{-1} due to the O-H stretching within the apatitic structure, its intensity is related to the crystallinity of the material and is much less intense, sometimes even completely masked by the water band, in the case of carbonated apatite.[45] Theoretically the phosphate groups would present 4 IR active modes: symmetric stretching υ_1, asymmetric stretching υ_3, symmetric bending υ_2 and asymmetric bending υ_4. Due to the presence of OH groups the phosphate ion is not of perfect T_d symmetry υ_3 and υ_4 are split into more than one band.[46]

4.5.2 X-ray diffraction pattern

The X-ray diffraction pattern of hydroxyapatite is shown in Figure 28. Data was normalized setting the most intense peak (31.81°) as 100%. Parameters of the unit cell can be determined from the powder X-ray diffraction pattern. Hydroxyapatite crystallizes in a hexagonal unit cell and the relationship between the Miller indices (hkl) and the distance d between planes is given

by Equation 6. Using Bragg's Law (Equation 5) this relationship becomes Equation 7 which relates the experimental diffraction angle θ_d and the Miller indices. With the Miller indices attributed to each Bragg reflection the lattice parameters a, b and c ($a = b$ in a hexagonal space group) can be determined.

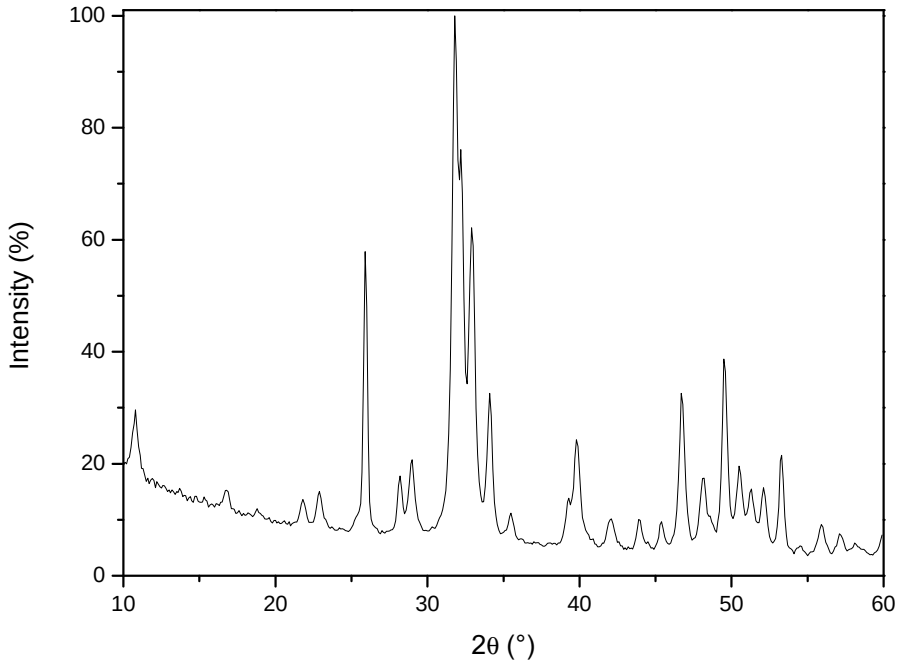

Figure 28: X-ray diffraction pattern of hydroxyapatite.

$$d = \frac{1}{\sqrt{\frac{4}{3} \cdot \frac{h^2+hk+l^2}{a^2} + \frac{l^2}{c^2}}} \tag{6}$$

$$\eta\mu^2\theta_d = \frac{\lambda^2}{4} \cdot \left(\frac{4}{3} \cdot \frac{h^2 + hk + l^2}{a^2} + \frac{l^2}{c^2} \right) \tag{7}$$

The Miller indices of hydroxyapatite were attributed[13] to the experimental reflections (Annex A) and the calculated cell parameters were $a = b = 9.422$ Å and $c = 6.881$ Å.

4.6 Synthesis of (9*R*)-9-hydroxystearic acid modified hydroxyapatite

The traditional direct synthesis[13,19] of hydroxyapatite is usually done with the slow addition of $(NH_4)_2HPO_4$ onto heated $Ca(NO_3) \cdot 4\,H_2O$. 9R-HSA-K should be added to the ammonium phosphate so that it is also slowly put into contact with the calcium ions. Initially this method was tested but proved to be unfeasible due to the precipitation of 9R-HSA-K in the addition funnel. The solution to this problem was the heating of ammonium phosphate and 9R-HSA-K with the slow addition of calcium nitrate.

4.6.1 Fourier-Transform Infrared spectrum

The infrared spectrum of (9R)-9-hydroxystearic acid modified hydroxyapatite (Figure 29, Table 2) is very similar to that of HSA with the addition of the most intense bands of potassium (9R)-9-hydroxystearate, notably the C-H stretching in the region between 2982 and 2823 cm^{-1} and the C=O stretching at 1551 cm^{-1}. The frequency of the C=O stretching is shifted towards lower wavenumbers than in 9R-HSA suggests that the acid is completely deprotonated, presenting the same frequency seen as in 9R-HSA-K.

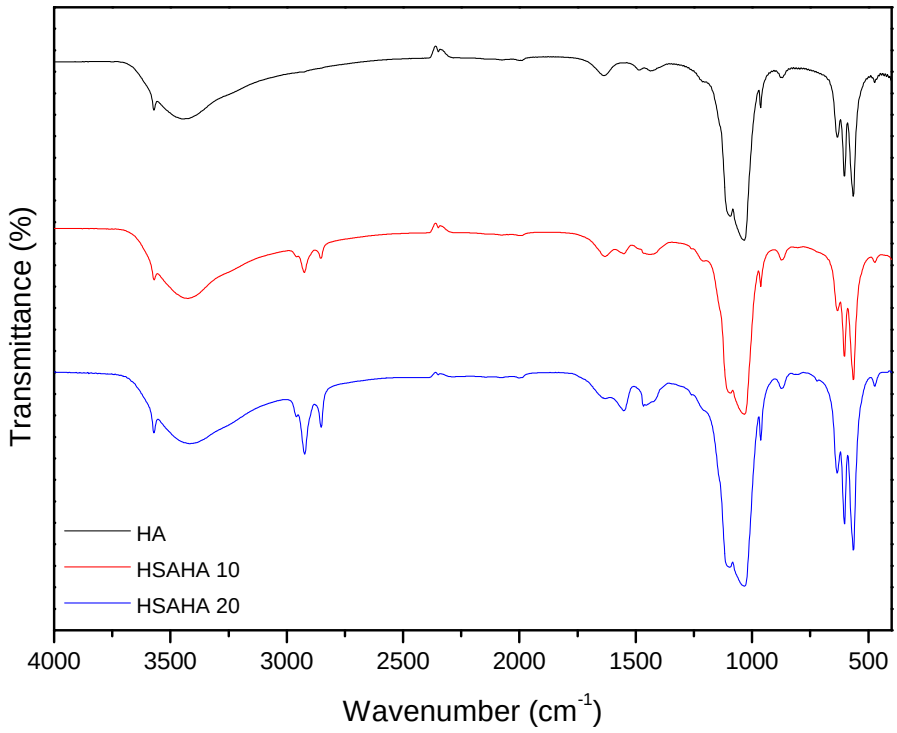

Figure 29: Infrared spectrum of hydroxyapatite with the addition of 0, 10 and 20 mM of (9R)-9-hydroxystearic acid.

Table 2: Infrared Absorption Spectroscopy Data for hydroxyapatite and (9R)-9-hydroxystearic acid modified hydroxyapatite.

Peak assignments	HA (cm^{-1})	HSA-HA (cm^{-1})
HA Hydroxyl stretch (m)	3569	3560
H_2O hydroxyl stretch (vb)	3700–3000	3700-3000
9R-HSA-K C-H stretch	–	2982–2823
Atmospheric CO_2	2394–2284	2391–2281
Carbonate υ_3 (m)[45]	1635	1632
9R-HSA-K C=O stretch	–	1551
Carbonate υ_3 (m)[45]	1486	1487
Carbonate υ_3 (m)[45]	1442	1442
Phosphate υ_3 (vs)[45]	1101	1096
Phosphate υ_3 (vs)[45]	1037	1032
Phosphate υ_1 (m)[45]	962	962
Carbonate υ_2 (ms)[45]	873	872
Phosphate υ_4 (m)[45]	633	633
Phosphate υ_4 (vs)[45]	602	603
Phosphate υ_4 (vs)[45]	566	564
Phosphate υ_2 (w)[45]	475	472

(vs) very strong, (ms) medium strong, (m) medium, (w) weak, (vb) very broad

4.6.2 X-ray diffraction pattern

The X-ray diffraction pattern of (9*R*)-9-hydroxystearic acid modified hydroxyapatite (Figure 30) is similar to that of hydroxyapatite without notable shift, suggesting that the lattice parameters are maintained with the addition of 9R-HSA-K to HA. A slight broadening of the peaks is visible, suggesting that the crystal size of the modified HA is reduced.

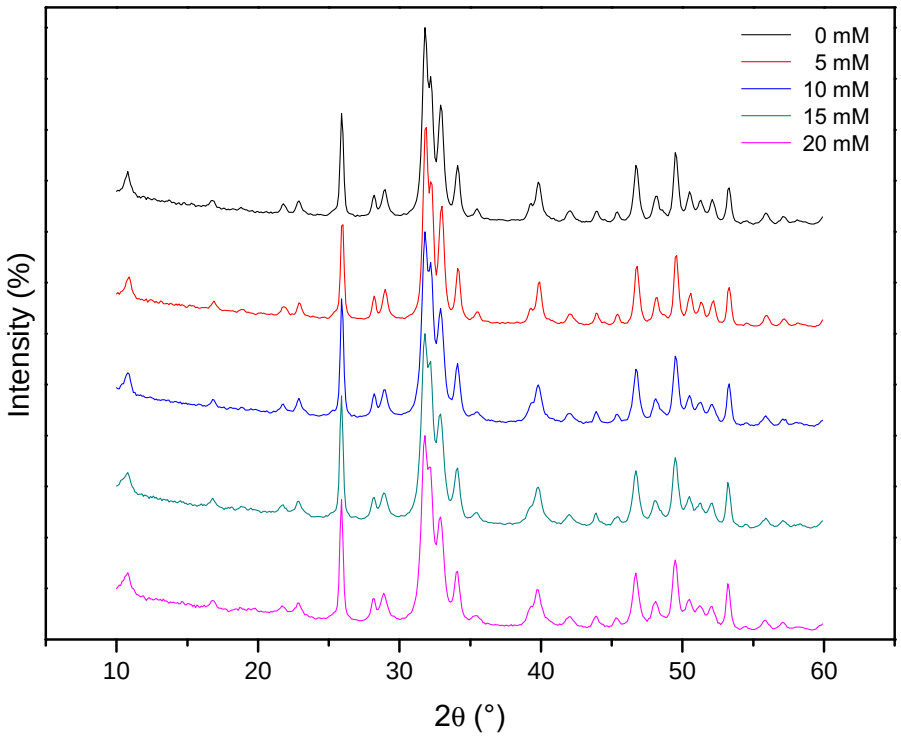

Figure 30: Comparison between X-ray diffraction patterns for hydroxyapatite and (9*R*)-9-hydroxystearic acid modified hydroxyapatite.

From the diffraction pattern the cell parameters obtained are shown in Table 3. A slight increase of a from 9.422 Å to 9.431 Å can be appreciated, however it is too small to be considered relevant because the increase in width of the peaks made measurement of their precise positions difficult. c remained essentially unchanged at 6.881 Å. Large changes in unit cell parameters would suggest incorporation of (9*R*)-9-hydroxystearic acid within the cell lattice, which probably does not happen due to 9R-HSA's large size. Since there is not a considerable change in the cell parameters there is no change in the cell volume.

Average crystallite size or coherent domain length (τ_{hkl}) can be determined using the Scherrer equation[47] (Equation 8) assuming that the microstrain is negligible.

$$\tau_{hkl} = \frac{k\lambda}{\beta \cos\theta} \tag{8}$$

where λ is the wavelength of the incident radiation (1.5418 Å for Cu Kα radiation), θ is the Bragg angle of the reflection being analyzed (half the value of 2θ), β is the full width at half maximum, twice the half width at half maximum that was obtained from the MARQFIT

Table 3: Cell parameters of hydroxyapatite and (9*R*)-9-hydroxystearic acid modified hydroxyapatite determined by X-ray diffraction.

Sample	a (Å)	c (Å)	Unit Cell Volume (Å^3)
HA	9.422(2)	6.881(2)	529.2(1)
HSAHA 5	9.426(3)	6.883(2)	529.7(3)
HSAHA 10	9.431(3)	6.880(2)	529.8(2)
HSAHA 15	9.431(2)	6.881(2)	530.1(3)
HSAHA 20	9.430(2)	6.880(2)	529.8(3)

program. k is a constant that depends on the particle shape. It can vary from 0.7 to 1.7 and is usually 0.9 for hydroxyapatite. To obtain the corrected values of β, the instrumental broadening is corrected with the HWHM found experimentally for crystalline silicon (0.04°) using Equation 9. The error of τ_{hkl} (E) can be calculated using Equation 10 where $\delta_{\frac{1}{2}}$ is the error of the measurement of the HWHM.

$$\beta_{\frac{1}{2}corr} = \sqrt{\beta_{\frac{1}{2}}{}^2 - \beta_{\frac{1}{2}Si}{}^2} \tag{9}$$

$$E = \frac{\delta_{\frac{1}{2}}}{\beta_{\frac{1}{2}corr}} \cdot \tau_{hkl} \tag{10}$$

Coherent crystalline domain lengths are shown in Table 4. The increase of the width of the Bragg reflections with the increase of the concentration of potassium (9*R*)-9-hydroxystearate suggests that the average dimensions of the crystals decrease (Figure 31). The decrease is more pronounced for the (310) dimension of the crystallites, which decreases by 29.0% in size, while the already longer (002) length of the crystallites only decreases by 16.6% in size. This shows an anisotropy in the adsorption of the acid onto hydroxyapatite, a preference for the surfaces perpendicular to the *c*-axis, whose growth are inhibited, as has been reported for the synthesis of HA modified with acidic amino acids.[48]

Table 4: Coherent domain length τ_{hkl} determined by X-ray diffraction.

	Reflection 002				Reflection 310			
Sample	$\frac{1}{2}\beta$ (°)	$\frac{1}{2}\beta_{corr}$ (°)	β (°)	τ (Å)	$\frac{1}{2}\beta$ (°)	$\frac{1}{2}\beta_{corr}$ (°)	β (°)	τ (Å)
HA	0.0803(8)	0.0696(8)	0.1392	615(4)	0.194(2)	0.190(2)	0.3797	421(2)
HSAHA 5	0.0842(8)	0.0741(8)	0.1482	578(3)	0.194(2)	0.190(2)	0.3878	412(2)
HSAHA 10	0.0780(7)	0.0670(7)	0.1339	640(3)	0.222(2)	0.218(2)	0.4367	366(2)
HSAHA 15	0.858(7)	0.0757(7)	0.1514	566(3)	0.264(2)	0.261(3)	0.5219	306(2)
HSAHA 20	0.0926(7)	0.0835(7)	0.167	513(2)	0.270(3)	0.267(3)	0.5340	299(2)

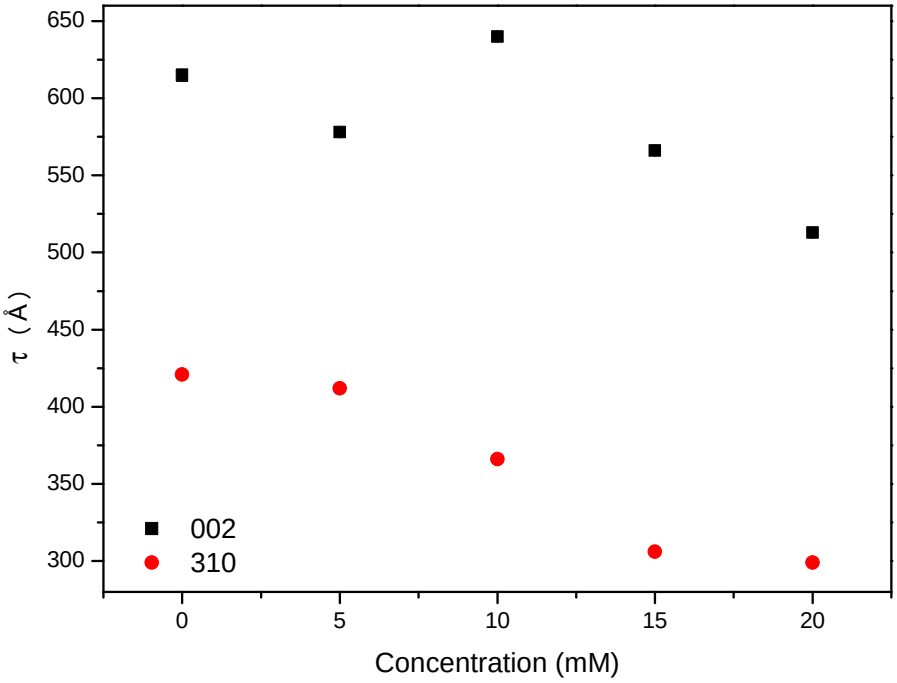

Figure 31: Average crystallite size (τ) measured from the (002) and (310) reflections as a function of the concentration of 9R-HSA-K in the synthesis.

4.6.3 Thermogravimetric analysis

The thermogravimetric analysis of (9*R*)-9-hydroxystearic acid modified hydroxyapatite (Figures 32 and 33) showed three regions of mass loss. The first one between room temperature and 200°C is the loss of absorbed water molecules and corresponds to about 2% of the mass of the material. The second mass loss, between 200°C and 600°C can be attributed to the mass loss of HA (pure HA loses approximately 2.5%) and the mass of 9R-HSA associated with HA (9R-HSA decomposes completely before 600°C). The third mass loss, between 700°C and 900°C is due to the loss of carbon dioxide gas, due to incorporated carbonate and is always less than 0.5% in weight. Table 5 shows that the amount 9R-HSA associated to hydroxyapatite increases up to 8.58% as a function of its concentration in solution.

Table 5: Thermogravimetric analysis of (9*R*)-9-hydroxystearic acid modified hydroxyapatite as a function of the concentration of 9R-HSA-K in the synthesis.

Sample	First mass loss (wt%)	Second mass loss (wt%)	Amount of HSA (wt%)
HA	1.9720	2.4655	0
HSAHA 5	1.8375	4.5413	2.0758
HSAHA 10	2.1295	6.8643	4.3988
HSAHA 15	1.8314	8.9956	6.5301
HSAHA 20	1.8978	11.0462	8.5807

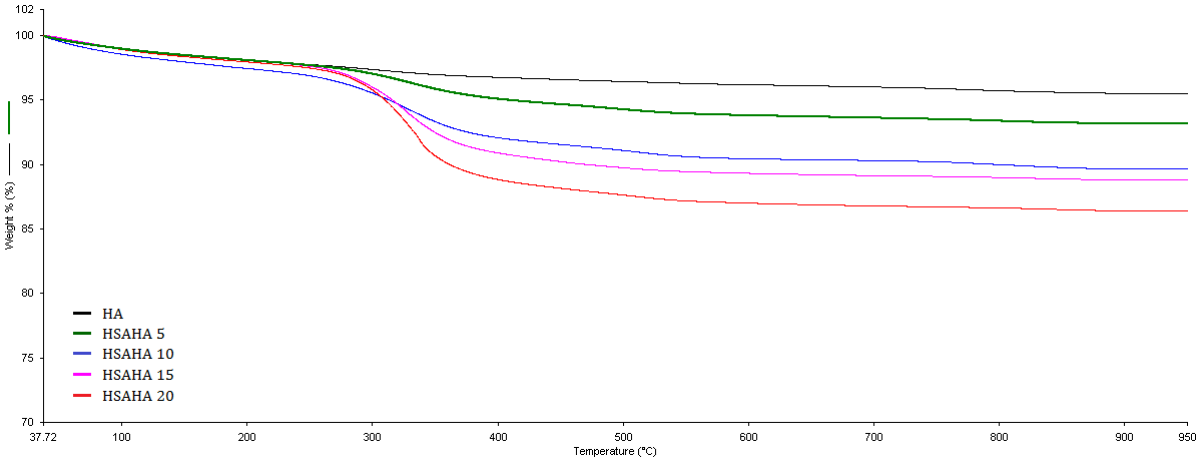

Figure 32: Thermogravimetric analysis of (9*R*)-9-hydroxystearic acid modified hydroxyapatite. Increasing concentrations of 9R-HSA-K are shown: 0 mM (black), 5 mM (green), 10 mM (blue), 15 mM (magenta) and 20 mM (red).

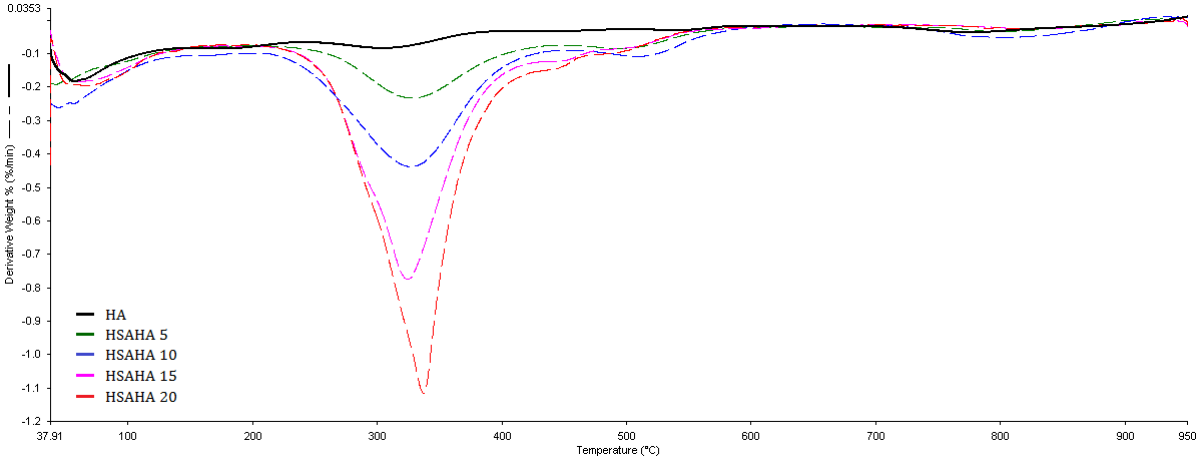

Figure 33: Differential thermal analysis of (9*R*)-9-hydroxystearic acid modified hydroxyapatite. Increasing concentrations of 9R-HSA-K are shown: 0 mM (black), 5 mM (green), 10 mM (blue), 15 mM (magenta) and 20 mM (red).

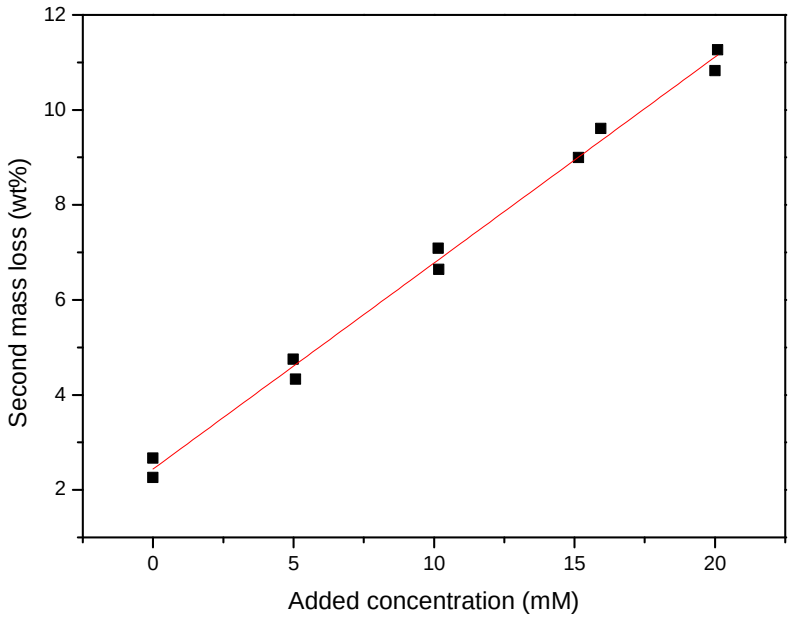

Figure 34: Increase of the second mass loss in the TGA as a function of the added amount of 9R-HSA-K. This shows a linear relationship and that no plateau was reached.

4.6.4 Transmission Electron Microscopy

Transmission Electron Microscopy grids were prepared for samples HA, HSAHA 10 and HSAHA 20. Images are shown in Figure 35.

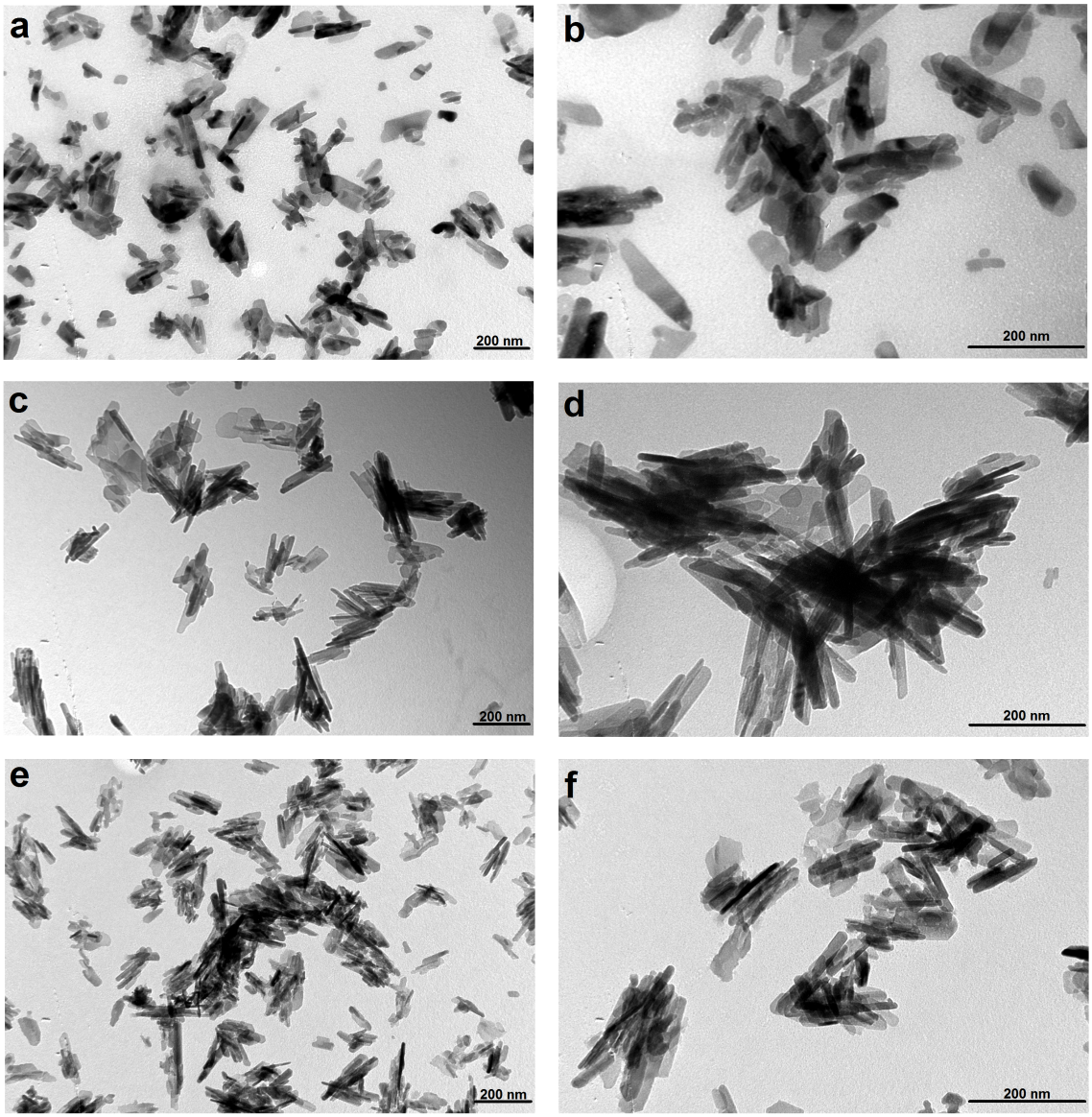

Figure 35: Transmission Electron Microscopy images of HA (a, b); HSAHA 10 (c,d) and HSAHA 20 (e,f). All scale bars represent 200 nm.

Table 6: Average crystal dimensions determined by Transmission Electron Microscopy.

Sample	Length (nm)	Width (nm)	Length to Width ratio
HA	215	65	3.3
HSAHA 10	142	28	5.2
HSAHA 20	68	13	5.2

No amorphous material was seen in the TEM images. Pure HA crystals present average dimensions of 215 nm by 65 nm (Table 6). There is a significant decrease in crystal size to 68 nm by 13 nm with the addition of 20 mM of hydroxystearic acid to the reaction. The slight change in synthesis method (slowly adding calcium nitrate to ammonium phosphate as opposed to the contrary) does not significantly change the morphology or size of the pure hydroxyapatite crystals. Incorporation of (9*R*)-9-hydroxystearic acid increases the length to width ratio of the crystals suggesting that there is a preferred adsorption surface for the acid, inhibiting growth on that surface. Assuming the length (longer dimension) of the crystal is parallel to the *c*-axis of the unit cell, the acid adsorbs on the (100) surface of the crystal. This is in agreement with previous studies[48–50] that show that organic acids preferentially adsorb onto the (100) surface where calcium ions are more accessible to coordination by the carboxylate group.

4.6.5 Contact Angle Measurement

Contact Angle is a type of measurement obtained to determine the wettability of a surface with respect to a specific liquid. In the case of water, a wettable surface is termed hydrophilic and a non-wettable surface is called hydrophobic. The measurement is done by adding a drop of the liquid to a flat surface and determining the angle where the liquid/air interface meets the solid surface. The value of the contact angle reflects the relative strength of the molecular interactions between the liquid/air and liquid/solid interfaces.[51] Since in all our measurements the liquid and air was kept the same, a change in the value of the contact angle represents a change in the molecular interactions at the liquid/solid interface.

Hydroxyapatite is very hydrophilic and therefore shows a very low contact angle (as shown in Figure 36: 0.33 s after the drop has touched the surface its contact angle is 7° and by 4 s water has been totally spread on the surface of the material. Even a low concentration of (9*R*)-9-hydroxystearic acid causes a huge change in the liquid/solid molecular interactions of this surface. The contact angle increases to 69° with 5 mM of 9R-HSA and once 10 mM have been added, the contact angle reaches a maximum of about 91°. In all samples containing 9R-HSA the surface contact angle was constant during the 30 s of acquisition. Samples with a surface contact angle of 90° or more are considered to be hydrophobic.

This experiment shows that the hydrophobic tails of 9R-HSA are what is on the surface of the material, in agreement with the idea that the charged carboxylate head is interacting with the calcium ions in hydroxyapatite. It is not known how the increased hydrophobicity will affect the material's activity but there are examples in the literature that show that osteoblast adhesion is increased with the decrease of the wettability.[52–54]

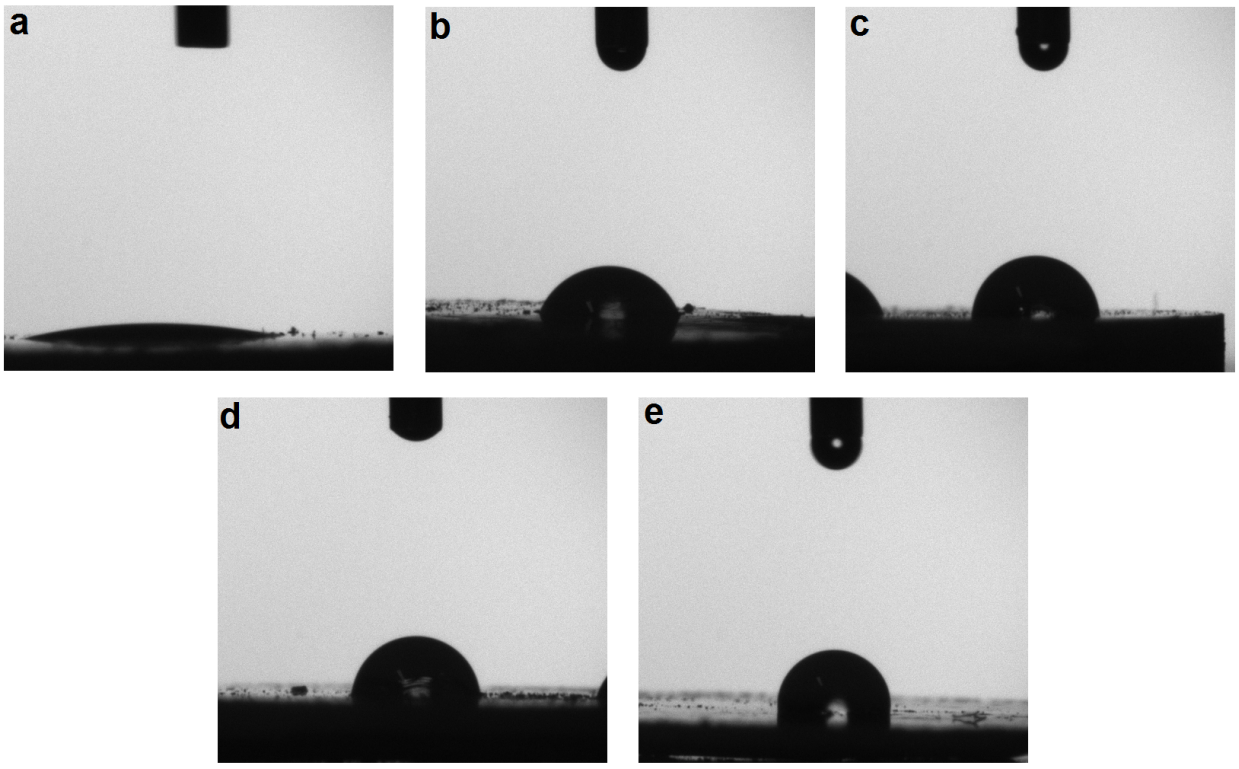

Figure 36: Contact Angle measurements for HA (a), HSAHA 5 (b), HSAHA 10 (c), HSAHA 15 (d) and HSAHA 20 (e). The contact angle rapidly increases with the addition of 9R-HSA, but reaches a maximum at HSAHA 10.

Table 7: Values of the contact angle for hydroxyapatite and (9R)-9-hydroxystearic acid modified hydroxyapatite taken 0.33s after the contact of the water droplet.

Sample	Contact Angle (°)
HA	7
HSAHA 5	69
HSAHA 10	91
HSAHA 15	93
HSAHA 20	92

4.6.6 Zeta potential determination

In a colloidal solution one factor that affects the lability of particles is the presence of charge on their surface. Ions of opposite charge tend to cluster nearby forming a layer called the interfacial double layer, due to the presence of ions of both charges organizing themselves around the particle. The inner layer of ions is non-mobile with respect to the particle and the radius of this rigid layer is called the 'shear radius'. The electric potential at the shear radius is what is known as the zeta potential or electrokinetic potential.[32]

Electrophoresis is used to determine the zeta potential of a charged particle because the zeta potential is related to the mechanical force applied on the particle when there is a difference of potential applied to it.[55] The zeta potential gives a relative quantification of the charge on the surface of the particle, as well as the sign of this charge.

Table 8: Zeta potential for hydroxyapatite and (9*R*)-9-hydroxystearic acid modified hydroxyapatite.

Sample	Zeta Potential (mV)
HA	-12.5
HSAHA 5	-17.8
HSAHA 10	-19.0
HSAHA 15	-20.4
HSAHA 20	-20.6

The zeta potential becomes more negative with the addition of 9R-HSA (Table 8), in agreement with the idea that the negatively charged carboxylate binds to the positively charged Ca^{2+} ions on the surface of HA. The zeta potential does not grow linearly with the increase of the amount of 9R-HSA and seems to be reaching a maximum at around -21 mV. Increased charge on the surface of HA has been shown to improve osteobonding in dog bone.[56,57]

4.6.7 Specific surface Area Measurement

Specific surface area is determined by the physical adsorption of a gas on the surface of a solid. The volume of gas adsorbed corresponding to a monomolecular layer is what is determined by the equipment and can be converted to area.

The values of the specific surface area for HA, HSAHA 5, HSAHA 10, HSAHA 15 and HSAHA 20 are shown in Table 9. The variation obtained in the measurements are within experimental error (10%) and therefore we cannot conclude from this experiment that there is a significant change in the surface area. The materials present a surface area of 49±5 m^2/g.

Table 9: Specific surface area of hydroxyapatite and (9R)-9-hydroxystearic acid modified hydroxyapatite.

Sample	Surface Area (m^2/g)
HA	56
HSAHA 5	48
HSAHA 10	42
HSAHA 15	48
HSAHA 20	50

5 Conclusions

(9*R*)-9-hydroxyoctadecanoic acid or (9*R*)-9-hydroxystearic acid (9R-HSA) was successfully prepared by conversion of dimorphecolic acid, a fatty acid contained in high concentration in *Dimorphotheca sinuata* L. seeds. Once the fatty acids belonging to the seed's triglycerides have been transesterified to the methyl esters, unsaturated fatty acids, including methyl dimorphecolate, are reduced with H_2 using Adam's catalyst PtO_2 and separated from the other methyl esters by column chromatography. The enantiomeric ratio of methyl 9-hydroxystearate was found to be 90:10 (R:S) by derivatization using (*R*)-(-)-O-acetylmandelic acid. 9R-HSA is obtained by hydrolyzing this methyl ester. The use of the enantio-enriched product is because it has been shown that the *R*-enantiomer is more active as a histone deacetylase inhibitor. These products were characterized mainly by nuclear magnetic resonance and mass spectrometry.

Since the hydroxyapatite synthesis is carried out in water, the first challenge in this work was solubilize 9R-HSA in water. This was done by preparing several salts from this acid. Potassium (9*R*)-9-hydroxystearate was chosen to be used because it proved to be the most soluble in water but still depends on high temperatures to be completely solubilized.

Hydroxyapatite (HA) was synthesized by the slow addition of calcium nitrate tetrahydrate to diammonium hydrogen phosphate in stoichiometric proportions under nitrogen gas flow to obtain a pure crystalline product. Typically this reaction is carried out by the slow addition of diammonium hydrogen phosphate to calcium hydrate tetrahydrate but this needed to be inverted to later include 9R-HSA in the synthesis. This change did not produce significantly different HA crystals.

9R-HSA was incorporated into HA by the inclusion of potassium (9*R*)-9-hydroxystearate in the HA synthesis, mixed with the diammonium hydrogen phosphate. The amount of 9R-HSA incorporated into HA is a function of the concentration in the reaction solution and it increases up to 8.58% in weight without precipitation of amorphous material. Coherent domain size and TEM images show a general decrease in crystal size with the addition of 9R-HSA. This decrease is more pronounced along the *a*-axis of the crystals, we can hypothesize that the carboxylate groups coordinate preferably to the 100 surface of the crystal, where the Ca^{2+} ions are more exposed, as has been shown for other carboxylic acids.[48] Contact angle measurements showed that the incorporation of 9R-HSA converts the typically hydrophilic HA into a hydrophobic material, with a maximum of 91° already reached at 4.5% wt 9R-HSA content. Similarly, the zeta potential also becomes more negative with the addition of 9R-HSA but is close to the maximum with 4.5% wt 9R-HSA content. Specific surface area measurements do not show significant changes with the addition of 9R-HSA.

In conclusion, 9R-HSA was successfully incorporated into HA. This has been shown to provoke the variations of several properties of the final apatitic materials, although these variations are not always proportional to the amount of associated 9R-HSA.

References

[1] Jane B. Reece, Lisa A. Urry, Michael L. Cain, Steven A. Wasserman, Peter V. Minorsky, Robert B. Jackson, and Neil A. Campbell. *Campbell Biology*. Benjamin Cummings, nineth edition, 2011.

[2] G. Farruggia, M. Casamenti, C. Castelluccio, C. Boga, and L. Masotti. 9-hydroxystearic acid elicits activation induced cell death in jurkat J6 cells. In *Italian Biochemical Society Transaction*, volume 15, page A132, Napoli, 2000. Società Italiana di Biochimica e Biologia Nazionale.

[3] N. Calonghi, E. Pagnotta, C. Parolin, C. Molinari, C. Boga, F. Dal Piaz, G.L. Brusa, M.A. Santucci, and L. Masotti. Modulation of apoptotic signalling by 9-hydroxystearic acid in osteosarcoma cells. *Biochimica et Biophysica Acta*, 1771:139–146, 2007.

[4] Carola Parolin, Natalia Calonghi, Enrica Presta, Carla Boga, Paolo Caruana, Marina Naldi, Vincenza Andrisano, Lanfranco Masotti, and Giorgio Sartor. Mechanism and stereoslectivity of HDAC I inhibition by (*R*)-9-hydroxystearic acid in colon cancer. *Biochimica and Biophysica Acta*, 1821:1334–1340, 2012.

[5] C. R. Smith, Jr, T. L. Wilson, E. H. Melvin, and I. A. Wolff. Dimorphecolic acid – a unique hydroxydienoid fatty acid. *Journal of the American Chemical Society*, 82(6):1417–1421, 1960.

[6] Cynthia Ebert, Fulvia Felluga, Cristina Forzato, Marco Foscato, Lucia Gardossi, Patrizia Nitti, Giuliana Pitacco, Carla Boga, Paolo Caruana, Gabriele Micheletti, Natalia Calonghi, and Lanfranco Masotti. Enzymatic kinetic resolution of hydroxystearic acids: A combined experimental and molecular modelling investigation. *Journal of Molecular Catalyis B: Enzymatic*, 83:38–45, 2012.

[7] Paolo Caruana. Sintesi di acido 9-idrossistearico e suoi derivati plurideuterati in forma racemica e, attingendo al *pool chirale* presente in natura, nelle due forme otticamente pure. Bachelor's thesis (*Tesi di Laurea*), Facoltà di Chimica Industriale – Università di Bologna, Bologna, Italy, 2006.

[8] Giuseppina Barrera, Stefania Pizzimenti, and Mario Umberto Dianzani. Lipid peroxidation: control of cell proliferation, cell differentiation and cell death. *Molecular Aspects of Medicine*, 29, 2008.

[9] Natalia Calonghi, Concettina Cappadone, Eleonora Pagnotta, Carla Boga, Carlo Bertucci, Jessica Fiori, Gianluca Tasco, Rita Casadio, and Lanfranco Masotti. Histone deacetylase 1: a target of 9-hydroxystearic acid in the inhibition of cell growth in human colon cancer. *Journal of Lipid Research*, 46:1596–1603, 2005.

[10] G. Cavalli, E. Casali, A. Spisni, and L. Masotti. Identification of the peroxidation product hydroxystearic acid in Lewis lung carcinoma cells. *Biochemical and Biophysical Research Communications*, 178(3):1260–1265, August 1991.

[11] N. Calonghi, C. Cappadone, E. Pagnotta, G. Farruggia, F. Buontempo, C. Boga, G. L. Brusa, M. A. Santucci, and L. Masotti. 9-hydroxystearic acid upregulates $p21^{WAF1}$ in HT29 cancer cells. *Biochemical and Biophysical Research Communications*, 314(1):138–142, 2004.

[12] Jennifer Kirkham. The crystals within. http://www.whatayear.org/03_12.php. Online; accessed 30-May-2014.

[13] S. Koutsopoulos. Synthesis and characterization of hydroxyapatite crystals: A review study on the analytical methods. *Journal of Biomedical Materials Research*, 62(4):600–612, December 2002.

[14] Yasuhiko Abe, Yohei Okazaki, Kyou Hiasa, Keisuke Yasuda, Keisuke Nogami, Wataru Mizumachi, and Isao Hirata. Bioactive surface modification of hydroxyapatite. *BioMed Research International*, 2013:9 pages, 2013. Article ID 626452.

[15] Toshiyuki Ikoma, Atsushi Yamazaki, Satoshi Nakamura, and Masaru Akao. Phase transition of monoclinic hydroxyapatite. *Netsu Sokutei*, 25(5):141–149, 1998.

[16] M. I. Kay, R. A. Young, and A. S. Posner. Crystal structure of hydroxyapatite. *Nature*, 204:1050–1052, December 1964.

[17] Aaron S. Posner, Alvin Perloff, and Alfred F. Diorio. Refinement of the hydroxyapatite structure. *Acta Crystallographica*, 11:308–309, 1958.

[18] H. McDowell, T. M. Gregory, and W. E. Brown. Solubility of $Ca_5(PO_4)_3OH$ in the system $Ca(OH)_2$-H_3PO_4-H_2O at 5, 15, 25 and 37°c. *Journal of Research of the National Bureau of Standards – A. Physics and Chemistry*, 81A(2–3), 1977.

[19] J. D. B. Featherstone, I. Mayer, F. C. M. Driessens, R. M. H. Verbeeck, and H. J. M. Heijligers. Synthetic apatites containing Na, Mg, and CO_3 and their comparison to tooth enamel mineral. *Calcified Tissue International*, 35:169–171, 1983.

[20] J. C. Elliot. *Structure and Chemistry of the Apatites and Other Calcium Orthophosphates.* Elsevier Science B. V., 1994.

[21] Joice Terra, Eric Rodrigues Dourado, Jean-Guillaume Eon, Donald E. Ellis, Gabriela Gonzalez, and Alexandre Malta Rossi. The structure of strontium-doped hydroxyapatite: an experimental and theoretical study. *Physical Chemistry Chemical Physics*, 11:568–577, 2009.

[22] Th. Leventouri, A. Antonakos, A. Kyriacou, R. Venturelli, E. Liarokapis, and V. Perdikatsis. Crystal structure studies of human dental apatite as a function of age. *International Journal of Biomaterials*, 2009:6 pages, 2009. Article ID 698547.

[23] Erzsébet-Sára Bogya, Réka Barabás, Alexandra Csavdári, Valentina Dejeu, and Ioan Bâldea. Hydroxyapatite modified with silica used for sorption of copper(II). *Chemical Papers*, 63(5):568–573, 2009.

[24] Qiyi Zhang, Yang Leng, and Renlong Xin. A comparative study of electrochemical deposition and biomimetic deposition of calcium phosphate on porous titanium. *Biomaterials*, 26:2857–2865, 2005.

[25] Adriana Bigi, Elisa Boanini, Barabara Bracci, Alessandro Facchini, Silvia Panzavolta, Francesco Segatti, and Luigina Sturba. Nanocrystalline hydroxyapatite coatings on titanium: a new fase biomimetic method. *Biomaterials*, 26:4085–4089, 2005.

[26] Centers for Disease Control and Prevention (CDC). Questions and answers about bone cancer. Online. http://www.cdc.gov/nceh/radiation/phase2/mbone.pdf.

[27] M. Stigter, K. de Groot, and P. Layrolle. Incorporation of tobramycin ito biomimetic hydroxyapatite coating on titanium. *Biomaterials*, 23:4143–4153, 2002.

[28] Y. Yamashita, A. Uchida, T. Yamakawa, Y Shinto, N. Araki, and K. Kato. Treatment of chronic osteomyelitis using calcium hydroxyapatite ceramic implants impregnated with antibiotic. *International Orthopaedics*, 22:247–251, 1998.

[29] Andrea Ewald, Daniel Hösel, Sarika Patel, Liam M. Grover, Jake E. Barralet, and Uwe Gbureck. Silver-doped calcium phosphate cements with antimicrobial activity. *Acta Biomaterialia*, 7(11):4064–4070, November 2011.

[30] Yaser Ghani, Melanie J. Coathup, Karin A. Hing, and Gordon W. Blunn. Development of a hydroxyapatite coating containing silver for the prevention of peri-prosthetic infection. *Journal of Orthopaedic Research*, 30(3):356–363, March 2012.

[31] Elisa Boanini, Paola Torricelli, Maria Cristina Cassani, Giovanna Angela Gentilomi, Barbara Ballarin, Katia Rubini, Francesca Bonvicini, and Adriana Bigi. Cationic-anionic polyelectrolyte interaction as a tool to graft silver nanoparticles on hydroxyapatite crystals and prevent cytotoxicity. *RSC Advances*, 4:645–652, 2014.

[32] Peter Atkins and Julio de Paula. *Atkins' Physical Chemistry.* Oxford University Press, Oxford, eighth edition, 2006.

[33] Raymond P. W. Scott. Analytical spectroscopy, March 2014. http://www.analyticalspectroscopy.net/ap7-3.htm.

[34] Gale Rhodes. *Crystallography Made Crystal Clear*. Academic Press, third edition, 2006.

[35] University of Iowa. Online, March 2014. http://www.uiowa.edu/ c004206/hand9.pdf.

[36] JCPDS International Centre for Diffraction Data. Online, 2014. http://www.icdd.com.

[37] Peter J. Goodhew, John Humphreys, and Richards Beanland. *Electron Microscopy and Analysis*. Taylor & Francis, third edition, 2001.

[38] David G. Hay. CELSIZ V1.1. Software, June 1995. http://www.iucr.org/resources/other-directories/software/celsiz.

[39] W. Schreiner, M. Kramer, S. Krischer, and Y. Langsam. MARQFIT. *PC Tech Journal*, 3(5):170–190, May 1985.

[40] C. C. Cochrane and H. J Harwood. Phase properties of mixtures of 9- and 10-oxo-octadecanoic acids and of 9- and 10-hydroxyoctadecanoic acids. *Journal of Organic Chemistry*, 26(4):1278–1282, April 1961.

[41] Robert M. Silverstein, Francis X. Webster, and David J. Kiemle. *Spectrometric Identification of Organic Compounds*. John Wiley & Sons, seventh edition, 2005.

[42] J. Cymerman Craig, S. K. Roy, R. G. Powell, and C. R. Smith Jr. Optical rotatory dispersion and absolute configuration. vi. structure and absolute configuration of helenynolic acid. *Journal of Organic Chemistry*, 30(12):4342–4343, December 1965.

[43] Francis A. Carey and Richard J. Sundberg. *Advanced Organic Chemistry*, volume B. Springer, New York, fifth edition, 2007.

[44] James K. Whitesell and Dan Reynolds. Resolution of chiral alcohols with mandelic acid. *Journal of Organic Chemistry*, 48(20):3548–3551, 1983.

[45] I. Rehman and W. Bonfield. Characterization of hydroxyapatite and carbonated apatite by photo acoustic FTIR spectroscopy. *Journal of Materials Science: Materials in Medicine*, 8:1–4, 1997.

[46] Ray L. Frost, Yunfei Xi, Ricardo Scholz, Fernanda Maria Belotti, and Andres Lopez. Infrared and raman spectroscopic characterization of the phosphate mineral fairfieldite – $Ca_2(Mn^{2+}Fe^{2+})_2(PO_4)_2 \cdot 2\,H_2O$. *Spectroscopica Acta Part A: Molecular and Biomolecular Spectroscopy*, 106:216–223, 2013.

[47] A. L. Patterson. The Scherrer formula for X-ray particle size determination. *Physical Review*, 56:978–982, 1939.

[48] Elisa Boanini, Paola Torricelli, Massimo Gazzano, Roberto Giardino, and Adriana Bigi. Nanocomposites of hydroxyapatite with aspartic acid and glutamic acid and their interaction with osteoblast-like cells. *Biomaterials*, 27:4428–4433, 2006.

[49] Adriana Bigi, Elisa Boanini, Massimo Gazzano, Marek A. Kojdecki, and Katia Rubini. Microstructural investigation of hydroxyapatite-polyelectrolyte composites. *Journal of Materials Chemistry*, 14:274–279, 2004.

[50] Su-Ping Huang, Ke-chao Zhou, and Zhi-you Li. Inhibition mechanism of aspartic acid on crystal growth of hydroxyapatite. *Transactions of Nonferrous Metals Society of China*, 17:612–616, 2007.

[51] Renate Förch, Holger Schönherr, and A. Tobias A. Jenkins. *Surface Design: Applications in Bioscience and Nanotechnology*, chapter Appendix C: Contact Angle Goniometry, pages 471–473. John Wiley & Sons, 2009.

[52] Monique Hott, Benoit Noel, Didier Bernache-Assolant, Christian Rey, and Pierre J. Marie. Proliferation and differentiation of human trabecular osteoblastic cells on hydroxyapatite. *Journal of Biomedical Materials Research*, 37:508–516, 1997.

[53] S. A. Redley, S. Razzouk, C. Rey, D. Bernache-Assollant, G. Leroy, M. Nardin, and G. Cournot. Osteoclast adhesion and activity on synthetic hydroxyapatite, carbonated hydroxyapatite, and natural calcium carbonate: Relationship to surface energies. *Journal of Biomedical Materials Research*, 45(2):140–147, 1999.

[54] Stéphane A. Redley, Michel Nardin, Didier Bernache-Assolant, Christian Rey, Philippe Delannoy, Laurent Sedel, and Pierre J. Marie. Behavior of human osteoblastic cells on stoichiometric hydroxyapatite and type A carbonate apatite: Role of surface energy. *Journal of Biomedical Materials Research*, 50:353–364, 2000.

[55] J. Lyklema, A de Keizer, B. H. Bijsterbosch, G. J. Fleer, and M. A. Cohen Stuart. *Fundamentals of Interface and Colloid Science.* Academic Press, 1995.

[56] Takayuki Kobayashi, Satoshi Nakamura, and Kimihiro Yamashita. Enhanced osteobonding by negative surface changes of electrically polarized hydroxyapatite. *Journal of Biomedical Materials Research*, 57:477–484, 2001.

[57] Satoshi Nakamura, Takayuki Kobayashi, and Kimihiro Yamashita. Extended bioactivity in the proximity of hydroxyapatite ceramic surfaces induced by polarization charged. *Journal of Biomedical Materials Research*, 61:593–599, 2002.

[58] A. P. Tulloch. Carbon-13 NMR spectra of all isomeric methyl hydroxy- and acetoxyoctadecanoates. *Organic Magnetic Resonance*, 11(3):109–115, 1978.

Annexes

A. Attribution of X-Ray diffraction pattern Bragg reflections

The experimental X-ray diffraction patterns were compared the standards contained in the International Centre for Diffraction Data (ICDD) database, using the 00-009-0432 card for synthetic hexagonal hydroxyapatite. This comparison permitted the attribution of the Miller indices to the experimental Bragg reflections, which was used to determine the unit cell parameters.

Table 10: Comparison of experimental Bragg reflections with those contained in ICDD card 00-009-0432.

Miller indices			Experimental		Reference		Miller indices			Experimental		Reference	
h	k	l	2θ (°)	d (Å)	2 θ (°)	d (Å)	h	k	l	2θ (°)	d (Å)	2 θ (°)	d (Å)
1	0	0	10.80	8.19	10.82	8.17	3	1	0	39.82	2.26	39.82	2.26
1	0	1	16.82	5.27	16.84	5.26	3	1	1	42.02	2.15	42.03	2.15
1	1	0	18.84	4.71	18.78	4.72	1	1	3	43.90	2.06	43.81	2.07
2	0	0	21.80	4.08	21.82	4.07	2	0	3	45.36	2.00	45.30	2.00
1	1	1	22.89	3.89	22.90	3.88	2	2	2	46.73	1.94	46.71	1.94
0	0	2	25.91	3.44	25.88	3.44	3	1	2	48.12	1.89	48.10	1.89
1	0	2	28.22	3.16	28.13	3.17	2	1	3	49.54	1.84	49.47	1.84
2	1	0	28.95	3.13	28.97	3.17	3	2	1	50.51	1.81	50.49	1.81
2	1	1	31.81	2.81	31.77	2.81	4	1	0	51.27	1.78	51.29	1.78
1	1	2	32.20	2.78	32.20	2.78	4	0	2	52.13	1.75	52.10	1.75
3	0	0	32.91	2.72	32.90	2.72	0	0	4	53.25	1.72	53.15	1.72
2	0	2	34.09	2.63	34.05	2.63	3	1	3	57.15	1.61	57.13	1.61
3	0	1	35.48	2.53	35.48	2.53	5	0	1	58.12	1.59	58.08	1.59
2	1	2	39.24	2.30	39.21	2.30							

B. Attribution of ^{13}C NMR peaks for 9R-HSA-Me and 9R-HSA

Attribution of the ^{13}C NMR peaks for both methyl (9R)-9-hydroxystearate (9R-HSA-Me) and (9R)-9-hydroxystearic acid have been attributed based on the values reported by Tulloch.[58] The carbon identifications are shown in Figure 37.

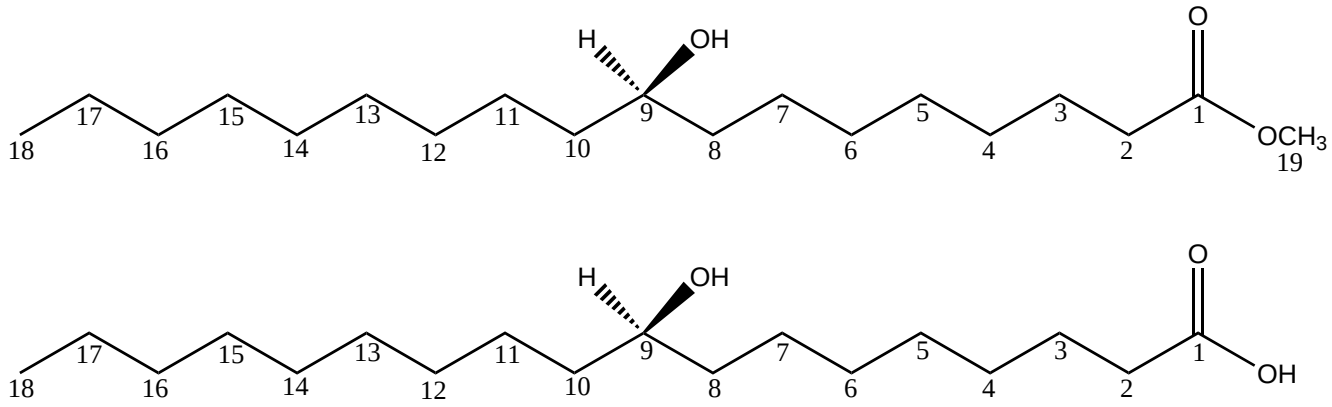

Figure 37: Identification of Carbons used in the ^{13}C NMR attribution.

Table 11: Attribution of the ^{13}C NMR peaks for methyl (9R)-9-hydroxystearate (9R-HSA-Me) and (9R)-9-hydroxystearic acid (9R-HSA).

Carbon	9R-HSA-Me (ppm)	9R-HSA (ppm)
1	174.1	178.7
2	33.9	33.5
3	24.8	24.8
4	28.9	28.9
5	29.1	29.2
6	29.4	29.4
7	25.4	25.5
8	37.3	37.4
9	71.7	72.0
10	37.4	37.5
11	25.5	25.7
12	29.6	29.7
13	29.56	29.6
14	29.5	29.6
15	29.2	29.2
16	31.8	31.9
17	22.6	22.7
18	14.05	14.1
19	51.3	–

C. List of Mass Spectrometry peaks of 9R-HSA-Me and 9R-HSA

Table 12: List of Mass Spectrometry peaks of methyl (9*R*)-9-hydroxystearate (9R-HSA-Me) and (9*R*)-9-hydroxystearic acid (9R-HSA). Spectra were obtained by EI-MS.

9R-HSA-Me		9R-HSA					
m/z	Rel. Height	m/z	Rel. Height	m/z	Rel. Height	m/z	Rel. Height
41.0121	20.54	39.016	2.90	73.0186	20.44	115.0630	2.92
42.9914	5.64	41.0316	26.48	74.0242	1.23	126.0912	3.04
43.0280	19.67	42.0387	5.43	79.0448	1.23	127.0990	10.45
55.0209	31.30	43.0105	5.36	81.0596	5.71	128.1027	1.03
56.9998	7.45	43.0469	25.71	82.0673	8.26	130.0858	1.61
57.0365	10.98	44.0176	2.94	83.0363	1.80	138.1277	3.42
67.0174	11.41	45.0258	3.37	83.0748	23.92	141.0773	4.25
69.0324	17.51	53.0302	1.60	84.0456	5.14	144.1009	15.39
73.9970	33.16	54.0377	3.07	84.0821	3.78	145.1066	2.19
81.0266	6.23	55.0091	2.93	85.0525	1.44	155.0937	100.00
83.0423	17.33	55.0456	36.70	85.0907	2.97	156.0937	9.82
86.9995	49.87	56.0525	6.18	87.0332	4.82	157.1443	3.15
95.0362	5.44	57.0248	9.19	93.0591	1.24	173.1017	13.18
97.0510	7.34	57.0612	13.03	95.0748	5.36	174.1056	1.33
101.0080	8.28	58.0318	1.65	96.0809	2.87	264.2275	1.77
109.0392	13.94	59.0399	2.93	97.0506	2.52		
115.0205	17.87	60.0116	9.46	97.0897	9.51		
129.0396	6.08	61.0184	1.07	98.0605	21.92		
155.0431	100.00	67.0445	12.09	99.0651	1.87		
156.0464	10.31	68.0519	5.17	101.0480	10.32		
158.0605	52.69	69.0603	22.37	109.0884	15.71		
159.0737	11.27	70.0666	3.96	110.0944	2.42		
187.0427	45.29	71.0394	3.26	111.0675	2.12		
188.0515	5.25	71.0755	4.15	111.1057	1.22		